CENTRO DE INVESTIGACIONES
EN OPTICA, A.C.

# “ANALYSIS AND CORRECTION OF THE ADDITIVE PHASE EFFECT GENERATED BY POWER CHANGE IN A MACH-ZEHNDER INTERFEROMETER INTEGRATED TO AN OPTICAL TRAP”

**Tesis que para obtener el grado de Doctor en Ciencias (Óptica)**

***Presenta: Azael David Domínguez Flores***

*Director de Tesis: Dr. Juan Antonio Rayas Alvarez*

“Versión definitiva. Incluye cambios sugeridos por revisores.”
Vo.Bo. Dr. Juan Antonio Rayas Alvarez

***León· Guanajuato· México***
***Mayo de 2024***

*“La ciencia siempre vale la pena porque sus descubrimientos, tarde o temprano, siempre se aplican.”*
Severo Ochoa

*To my parents,*

*Carmen Flores & David Domínguez*

# Acknowledgements

I would like to acknowledge CONAHCYT for the scholarship and their financial support (grant number 758043).

Thanks to Centro de Investigaciones en Óptica, A.C. (CIO) for giving me the opportunity to earn my Master's and PhD degrees as your student, for having provided me with the use of its facilities and for the human support of each one of its employees in the different departments. I also thank all the teachers who dedicated themselves to be part of my academic formation.

It is a real pleasure to express my deep gratitude to my PhD advisor, Dr. Juan Antonio Rayas, who gave me guidance throughout these years. Thank you for your patience, your time, your advice and for correcting me when necessary. It has been a privilege to be able to count on your support.

Thanks to Dr. Francisco Cuevas de la Rosa, Dr. Socorro Hernández Montes, Dr. Noé Alcalá Ochoa and Dr. Amalia Martínez García; for having been the follow-up committee and examiners of this project throughout the doctoral program. Thanks for your attention and time.

Thanks to my colleagues in the Grupo de Pruebas Ópticas y Mecánicas, especially Karen Reyes, Analia Sicardi, Iván Hernández and Kenia Rodríguez; for their contributions inside and outside of the lab.

Thanks to Chris Albor for her support in the use of the scanning electron microscope (SEM) and other equipment.

Thanks to Mario Ruiz for reviewing the use of English in this thesis, which helps to improve this work.

Thanks to Dr. Salvador Fernández Tavizón†, Maiby Valle-Orta and Uriel Sierra from Laboratorio Nacional de Materiales Grafénicos of Centro de Investigación en Química Aplicada (CIQA); for the synthesis and suspension of the graphenic material.

Thanks to Dr. José Luis Maldonado, Martín Olmos and Alvaro Guerra-Him; for their technical support and discussion in this work.

I am deeply grateful to my family: my sister Carmen Edith, my parents Carmen and David, my brother Iván, my grandma Aurora, my aunts Mayi and Norma; for their understanding, motivation and unconditional trust.

Thanks to the friends that I made during my time in CIO: Daniel Gómez, Natalith Palacios, Daniel Luis, Iván Choque, Edgar Reyes, Diana Mancera, Astrid Jordana del Socorro Saldaña Sánchez, Saraí Domínguez and those whom I have not mentioned due to insufficient paper. Thank you for all the doubts clarified, for your words of encouragement, for your company, advices, talks and funny moments. Thank you for sharing a little bit of yourselves with me.

Finally, thanks to my friends who, from a distance, I continue to count on them: Rocío, Emilio, Diego, Lis, Faby and Naye.

# Abstract

Immersion microscope objectives stand out for their large numerical aperture, which improves the optical resolution of imaging systems such as those used in microscopic interferometry. At the same time, these objectives make it possible to increase the gradient forces of a beam focused through them, thus forming an Optical Trap (OT). However, many studies on microscopic interferometry neglect the contributions of different optical materials of the system that are also exposed to laser radiation. In this work, a Mach-Zehnder interferometer and an optical trap, that share several components (including the same oil immersion objective), were coupled. Here an individual analysis of the media through which light travels and which are present in the experimental setup is carried out to determine their optical contributions to the experimental performance and results. Also, it is reported the response of interferometer (phase shifting in interference fringes) to a progressive increasing in the optical trap laser power, while the interferometer laser power remains constant. When a change in laser power is applied, the oil temperature changes, and consequently, so does its refractive index and volume, which in turn causes a phase shifting on the transmitted wavefront. The study here presented suggests that the refractive index variations in the immersion oil affect interferograms because they will then exhibit an additive phase term that must be considered in that final measurement. Moreover, the optical trap geometry will also change with the power increase. In order to make a proper digital correction, the laser characteristics and the oil response to its exposure must to be known. In the second part of this thesis, an optical phase analysis is applied in the three-dimensional measurement of the damage produced by the optical trap on a paint film so that the digital correction can be made later.

# Contents

I. Introduction ..... 1
II. Optical Techniques ..... 4
*II.I. Principles of interferometry* ..... 5
*II.II. Phase shifting algorithms (PSA)* ..... 7
*II.III. Optical microscopy* ..... 9
*II.IV. Optical trap* ..... 10
III. Optical Trap - Mach-Zehnder Interferometer Setup ..... 13
*III.I. Integration of Optical Trap and Interferometer* ..... 14
III.I.I. Optical trap setup ..... 14
III.I.II. Interferometer setup ..... 15
III.I.III. Integrated systems ..... 17
IV. Evaluation of Effect per Individual Media ..... 18
*IV.I. Identification of optical elements contributing to phase shifting* ..... 19
IV.I.I. Refractive index test ..... 21
IV.I.II. Temperature test ..... 23
IV.I.III. Volumetric test ..... 26
V. Calibration and Correction of the Additive Phase ..... 30
*V.I. Optical trap tests for phase calibration* ..... 31
*V.II. Additive phase correction* ..... 33
VI. Conclusions ..... 36
VII. Future Work ..... 39
References ..... 43
Appendix A: Achievements ..... 48

# List of figures

Figure 1. Examples of interferometers: a) Young's double-slit interferometer (wavefront-splitting), b) Michelson interferometer (amplitude-splitting). ..... 6
Figure 2. Mach-Zehnder interferometer (amplitude-splitting). ..... 7
Figure 3. Interferograms with phase shifting: a) $\phi$, b) $\phi + {}^{\pi}/_{2}$, c) $\phi + \pi$, d) $\phi + {}^{3\pi}/_{2}$, e) $\phi + 2\pi$.. ..... 8
Figure 4. Wrapped phase ($\phi_W$) from interferograms in Figure 3. ..... 9
Figure 5. Unwrapped phase ($\hat{\phi}$) from Figure 4. ..... 9
Figure 6. Role of immersion oil on a large numerical aperture microscope objective. In this representation, the dash-dotted line is the optical axis, the dashed line is the marginal ray collected by the objective and the dotted line is the missed marginal ray. ..... 10
Figure 7. Ray optics description of the gradient and scattering forces. The red arrows represent the main scattering forces, the gray arrows are the secondary scattering forces and gradient forces are depicted by green arrows. a) Unfocused beam and b) Focused beam by a lens. ..... 11
Figure 8. Representation of trapping regimes: a) Mie, b) Rayleigh. The red arrows represent the main scattering forces. ..... 12
Figure 9. Representation of the usual operation of an optical trap. (MO1—Condenser Microscope Objective, MO2—Oil Immersion Microscope Objective). a) Scheme, b) Experimental setup. In this setup, laser is redirected (by a dichroic beam splitter and a mirror) to MO2, which focuses the beam and forms the optical trap, then the beam continues its optical path, although it is no longer of interest for the experiment. Apart from that, white light is captured by MO1, illuminates the working area and continues its trajectory to form image in camera. ..... 14
Figure 10. Scheme of the Mach-Zehnder interferometer used. (MO1— Long Working Distance Microscope Objective, MO2—Oil Immersion Microscope Objective). ..... 15
Figure 11. System alignment. The intersection of the red lines indicates the center of the camera field of view and the yellow circle represents the optical trap position. ..... 16
Figure 12. Optical Trap - Mach-Zehnder interferometer setup. a) Experimental setup, b) Zoom where the Optical Trap is formed (region inside the yellow dotted line square in a)) and c) Scheme. (MO1—Long Working Distance Microscope Objective, MO2— Oil Immersion Microscope Objective).... 17
Figure 13. IR power required to cause a $2\pi$ shift depending on trap position. ..... 20
Figure 14. IR power required to cause a $2\pi$ shift with the trap located at −240 μm. The blue points indicate the average subtraction between interferograms with phase shifting and a reference. The red points indicate a maximum peak. ..... 20
Figure 15. Mach-Zehnder interferometer used to study refractive indices: a) Experimental setup photo, b) Scheme..... 21
Figure 16. Refractive index change when laser radiation excites: a) Air, b) Glass, c) Distilled water, d) Immersion oil..... 22
Figure 17. Behavior of the refractive index of the immersion oil and the working distance of an oil immersion objective. ..... 23
Figure 18. Experimental setup used to analyze thermal behavior: a) Photo, b) Scheme. ..... 24
Figure 19. Air and oil temperature profiles. Crossed-out readings indicate erratic thermocouple behavior..... 25

Figure 20. Oil temperature profile vs thermocouple position. Values showed as crossed out in Figure 19, here were removed and replaced for the interpolation curve. ..... 25
Figure 21. Comparison of thermal behavior and refractive index of oil over time. The asterisk indicates the point that was analyzed in Figure 16. ..... 26
Figure 22. Michelson interferometer used to study volume changes: a) Experimental setup photo, b) Scheme. ..... 27
Figure 23. Topography changes in time when laser radiation excites at: a) 5, b) 10, c) 15, d) 20, e) 25 and f) 30 seconds. ..... 28
Figure 24. Comparison of temperature, refractive index and volume change of the oil over time....28
Figure 25. Electron microscope images of a cross-sectional view of a paint film at magnifications of: a) 7,000X and b) 19,000X. ..... 31
Figure 26. Phase shifting (in profiles) relative to power shifting from 110 to 230 mW. ..... 32
Figure 27. Phase piston behavior in glass using 0 mW power as reference: a) Phase mapping, b) Profiles. ..... 32
Figure 28. Phase piston behavior in paint using 0 mW power as reference: a) Phase mapping, b) Profiles. ..... 33
Figure 29. Phase shifting behavioral trend shown in interferograms as well as in phase average (point) depending on the power. ..... 33
Figure 30. Paint damage (in phase terms) when the IR laser radiates at: a) 110; b) 140; c) 175; d) 205; and e) 230 mW. For each power, the greatest damage caused is observed in the yellow area…. ..... 34
Figure 31. Measurement correction of the phase map at 205 mW of power. Left side (from 0 to 4.78 µm over the *y*-axis) corresponds to the uncorrected phase and the right side (from 4.78 to 10.27 µm) is the corrected measurement. ..... 35
Figure 32. Graphene monolayer model with JSME Molecular Editor software. ..... 41
Figure 33. Phases of laser fragmentation of exfoliated graphene flakes suspended in water. a) Cavitation bubble generation, b) Fragmented nanoparticles generation. ..... 42
Figure 34. Fragmentation of exfoliated graphene flakes at different laser powers. a) 0 mW, b) 50 mW, c) 60 mW, d) 90 mW, e) 150 mW, f) 300 mW ..... 42

# *I.*

# *Introduction*

Optical trapping, is a technique used in various fields of science and engineering for manipulating microscopic objects with precision. This method utilizes highly focused laser beams to hold and study particles, cells, and molecules, [1] of course with their respective advantages and disadvantages. Some of the advantages offered by the optical trapping technique are precise control to manipulate, non-invasive, versatility to analyze different types of samples, real-time observation and high spatial resolution [2,3]. On the other hand, some known inherent disadvantages are having a limited range of trapping, potential sample damage depending on laser power and exposure time, sensitivity to environmental conditions and single-point manipulation [2,3]. The contribution of this work is the optical characterization of the immersion oil effects, used on some microscope objectives.

By knowing the properties of a material, they can be manipulated at a micro level to meet specific high-precision requirements. The present proposal is focused on the development of optical systems to know the mechanical behavior at the micro level of two-dimensional and quasi-two-dimensional structures. This work studies the effect of the radiation pressure of an optical trap to perform interferometric characterizations at micrometer scale by integrating two optical systems; a Mach-Zehnder interferometer and a conventional optical trap, where independent laser sources that share several optical components are used. Chapter II provides background information on the techniques used here. Among the shared elements in the optical trap and the interferometer is the oil immersion objective, which generates the optical trap; in Chapter III the systems are described separately, and then, their coupled implementation. However, it was detected that upon changing the power of either one of the two laser sources, the interferograms showed an additive phase shift; the cause and mechanism of this effect were unknown at the time. To the knowledge of the authors of this work, no reports have been found in literature that a change in the laser beam power of an optical trap generates any change in the phase of the wavefronts that are transmitted by the optical elements of the same trap.

In Chapter IV of this work, it is first described the method implemented to identify the contribution that each experimental arrangement component in common could have on the phase shifting observed; our experimental results have allowed us to determine that the phase shifting is caused by the oil immersion microscope objective. Consequently, a study of the optical, thermal and volumetric behavior of the oil implemented at macroscopic scale outside the trap-interferometer setup and exciting it with a higher power laser is shown below. The foregoing is also due to the fact that within the trap-interferometer setup it is not possible to individually analyze the oil characteristics. Although this analysis allows understanding the general behavior of immersion oil, the particular calibration on the optical trap must be implemented in-situ, as indicated below.

Chapter V presents a methodology to measure and correct the contribution of such additive phase when a change in laser source power is involved, due to some component from the optical tweezers or the interferometer, discarding that it be due to a direct contribution of the sample under study. In this case, the optical trap is used to generate damages on a black paint film at different powers, while interferometry is used to measure those damages due to thermal stress applied by the optical trap. Since the change in trap laser power adds a phase shifting to the interferograms, it is necessary to calibrate this additive phase term in the trap-interferometer system, to subsequently remove it from measurements.

Finally, in Chapter VII the proposal of a method to generate nanoparticles of graphenic materials from exfoliated graphene flakes suspended in water using the laser fragmentation technique is presented.

The constant miniaturization of electromechanical devices seeks to transform electronic systems in tasks as diverse as information processing, molecular manipulation and sensor fabrication. In recent decades, as devices continue to shrink in size and increase in operating frequency, new materials must be explored to meet future performance demands. One of the most important materials developments so far this century has been the discovery of two-dimensional materials. Since their discovery in 2004 [4], their properties and applications have been explored with emphasis mainly in areas including computer logic devices, niche applications within semiconductor technology and solar cells [5]. These materials have been studied in theory and in practice for several years at the Centro de Investigaciones en Óptica, A.C. from deposition methods [6], quantum methods related to photonics [7], its iteration with biological materials [8,9], even as temporary reinforcement of substrates [10], however, experiments based on non-invasive optical testing have yet to be explored.

For example, in terms of three-dimensional mechanical and geometric characterization of materials, a large variety of these have been performed on thin materials (membranes) at the Laboratory of Optical and Mechanical Testing (LABPOME) and its international collaborators have implemented optical systems for the topographic characterization of human skin [11] and fruit cuticles [12]. The morphological damage that red blood cells can suffer when subjected to aspiration and washing during cell rescue has even been studied, which in turn can lead to complications such as premature hemolysis (rupture) of the red blood cells [13,14].

# II.

# *Optical Techniques*

## *II.I. Principles of interferometry*

Light corresponds to a transverse wave behavior, since being an electromagnetic wave, its electric ($E$) and magnetic ($B$) fields are always perpendicular to the direction of propagation [15,16]. Mathematically, light can be described by a sine or cosine curve profile, due to the simplicity and cyclic properties of trigonometric functions [16]. Complex numbers are often used to represent wave functions. All such representations ultimately depend on a fundamental mathematical identity, known as Euler's theorem [15]. This is, in a spatially one-dimensional ($x$) example with time ($t$) dependence,

$$\psi(x,t) = A[\cos(\theta) + i\sin(\theta)] = Ae^{i\theta} = Ae^{i\left(\frac{2\pi}{\lambda}x - \omega t + \phi\right)}; \tag{1}$$

being $\psi$ the wave "displacement", $A$ represents the wave amplitude, $i = \sqrt{-1}$, $\theta$ is the phase information (or phase angle), $\lambda$ is the wavelength, $\omega$ is the angular speed (also called angular frequency) and $\phi$ is phase [15–17]. Phase is a particular characteristic of a wave cycle, usually expressed in terms of angular units. Phase changes are relevant in the context of the interference effects of light. The interference phenomenon occurs when two or more coherent waves, i.e., with the same wavelength, amplitude and linearly polarized planes of vibration, overlap in space [17,18]. Starting from Eq. (1), considering the amplitudes of two waves ($A_1$ and $A_2$) as electric fields ($E_1$ and $E_2$) and knowing that irradiance is the square of electric field, then it is possible to calculate the total radiant power density, or irradiance ($I$), of two waves on a point through

$$I = (\psi_1 + \psi_2)(\psi_1 + \psi_2)^* = I_1 + I_2 + 2\sqrt{I_1 I_2}\cos(\theta). \tag{2}$$

In Eq. (2), the spatial and time dependence $(x,t)$ is omitted for better visualization, $\psi_1$ and $\psi_2$ are two individual waves, and the asterisk indicates the complex conjugate of $(\psi_1 + \psi_2)$ where $i$ is replaced by $-i$, wherever it appears [16,17]. Also, $I_1$ and $I_2$ represent the irradiances of each wave. Although it is also possible to generate interference with incoherent light sources (or partially coherent sources), it is necessary to devise ways of producing mutually coherent waves [19]. Interference (constructive-destructive) can be observed in the form of bright and dark fringes (of irradiance) when projecting interfering beams onto a screen; this pattern is known as interference pattern [18]. Irradiance will reach a maximum value (bright fringe) when $\cos(\phi) = 1$, and will reach a minimum value (dark fringe) when $\cos(\phi) = -1$ in Eq. (2). If two waves in a vacuum interfere, the phase difference ($\Delta\phi$) with which they arrive at the interference point is due to the difference in the length of optical paths (OPD) traveled by each wave [19]. The phase difference can be measured to obtain very accurate metering information such as distance, refractive index and wavelength of the source [18]. An instrument designed to exploit the interference of light and the resulting fringe patterns for the purpose of making measurements in various quantities is called an optical interferometer [17]. The conditions for two waves to be mutually coherent were mentioned earlier, and this is only possible if they originate from the same source or if they are monochromatic and have exactly the same frequency, as in the case of some lasers [15]. Therefore, interferometers can be classified into two main groups, according to the method used [18–20]:

1. Wavefront-splitting interferometers.

2. Amplitude-splitting interferometers.

Wavefront-splitting interferometers can be realized by diffraction, reflection or refraction [15] and thus sample different light source portions propagated in the same direction [19]; Young's double-slit interferometer (Figure 1a) is the most representative of this category. As for amplitude splitting interferometers, they consist of splitting the wavefront into different portions (different amplitude, but without decreasing the extent of the wavefront) by using a birefringent element, a scattering grating/plate or a partially reflective film of a metal or dielectric (commonly called a beam splitter) to propagate the beams in different paths and then recombine them [15,18–20]; Michelson (Figure 1b) and Mach-Zehnder (Figure 2) interferometers are two well-known examples.

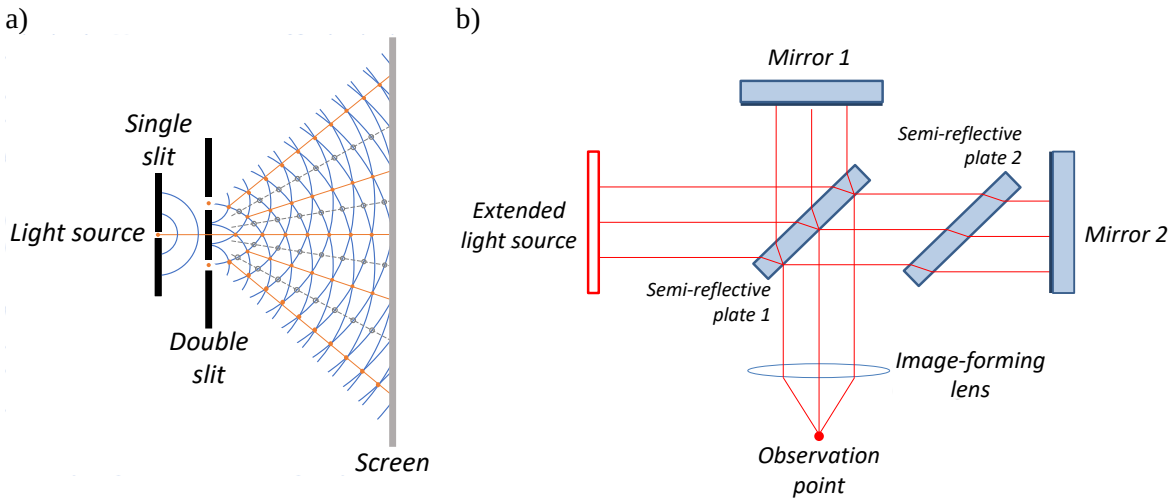


**Figure 1.** Examples of interferometers: a) Young's double-slit interferometer (wavefront-splitting), b) Michelson interferometer (amplitude-splitting).

For Young's interferometer, the phase difference is calculated by

$$\Delta\phi = \frac{2\pi}{\lambda} v \sin(\xi); \tag{3}$$

where $v$ is the distance between slits and $\xi$ is the angular spacing between the central bright fringe and a given point [16,17].

Whereas for a Michelson interferometer, the phase difference is

$$\Delta\phi = \frac{2\pi}{\lambda} 2l \cos(\delta); \tag{4}$$

being $l$ is the optical distance difference between the interferometer arms and $\delta$ is the angle of inclination of the beams with respect to the optical axis [16,17,19,20].

The interferometers used in the present work are the Michelson and Mach-Zehnder type. Therefore, below is the scheme of the Mach-Zehnder interferometer.

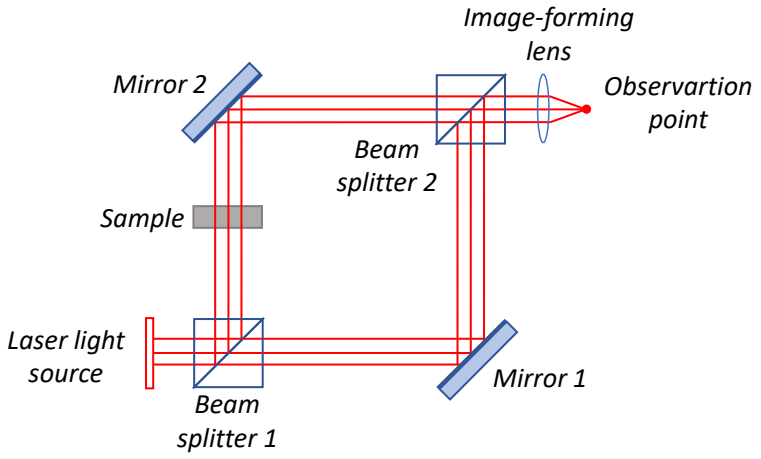


**Figure 2.** Mach-Zehnder interferometer (amplitude-splitting).

With this type of setup, the phase difference is obtained by

$$\Delta\phi = \frac{2\pi}{\lambda}\Delta n h; \tag{5}$$

here, $\Delta n$ is the refractive index difference between arms and $h$ is the sample thickness [20].

## *II.II. Phase shifting algorithms (PSA)*

Depending on the interference pattern type and the experimental conditions, the most appropriate method for the complete phase difference map calculation is selected; each method has its advantages and disadvantages. For example, when analyzing a dynamic sample whose interference generates open fringes, the Fourier method is commonly chosen because it requires only one interferogram [18]. On the other hand, if the sample is static or quasi-static and the interference fringes are closed, a phase shifting method is usually applied, which requires capturing several interferograms [18].

Multiple algorithms have been developed to estimate phase; in terms of phase shifting algorithms (PSA), and to mention a few, there are two, three, four and more steps [18,21]. Arbitrary phase shifts can be made and then estimated [22], however, it is recommendable to use constant phase steps to facilitate the analysis. [23].

An idealized model of an interference pattern with time-phase shifting modulation ($I(x,y,t)$) is described by

$$I(x,y,t) = a(x,y) + b(x,y)\cos[\phi(x,y) + \omega_0 t]. \tag{6}$$

Here, $a(x,y)$ is the background signal, $b(x,y)$ is the modulation signal (or fringe contrast), $\omega_0$ is a phase carrier and, for simplicity, I will henceforth refer to the phase difference (term of interest) as $\phi$. If the $I(x,y,t)$ term is known, a system of at least three equations is necessary to determine $\phi$, due to the infinite possibilities in the other parameters; in practice, it is common to introduce a variation that can be a sequential increase of $\omega_0 t = 2\pi t/N$ (also called "phase shifting" or "phase stepping"), being $N$ the total number of fringe patterns [21]. It is important to note that $t$ only indicates the instant at which the phase shifting is applied; it is not directly related to a specific time. Figure 3 shows five computer-simulated interferograms with a phase shifting of $\pi/2$.

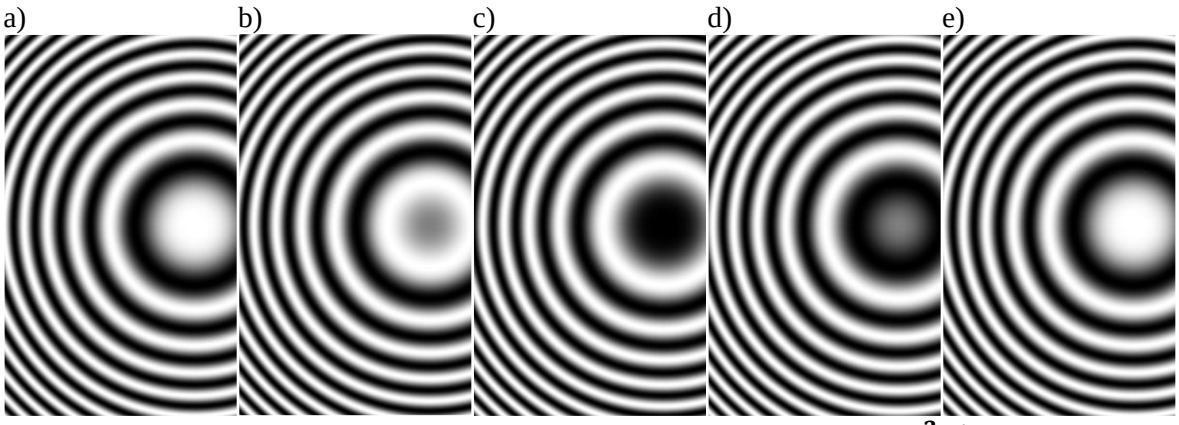


**Figure 3.** Interferograms with phase shifting: a) $\boldsymbol{\phi}$, b) $\boldsymbol{\phi + \pi/2}$, c) $\boldsymbol{\phi + \pi}$, d) $\boldsymbol{\phi + 3\pi/2}$, e) $\boldsymbol{\phi + 2\pi}$.

Experimentally, errors could be introduced during measurement (such as environmental disturbances, poor quality of the equipment used, temperature changes, etc.) that could cause a spatial variation of phase [21,24]. This would be, for example in Figure 3, that the phase stepping were different from $\pi/2$. Such a linear phase shifting miscalibration between measurements is called detuning. In this work, the 4-step +1 algorithm was used, since it is robust to detuning errors. So, wrapped phase ($\phi_W$) is given by [25]

$$\phi_W = \tan^{-1}\left(-\left[\frac{I_2 - I_4}{\frac{1}{2}I_1 - I_3 + \frac{1}{2}I_5}\right]\right), \tag{7}$$

being the interference pattern subscripts (1–5) the corresponding time step numbers, as related to Equation (6). Figure 4 corresponds to the obtained wrapped phase from interferograms in Figure 3.

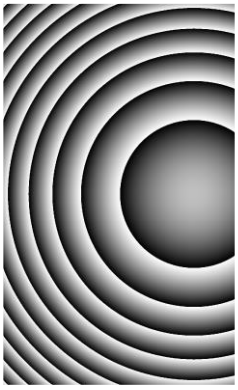

**Figure 4.** Wrapped phase ($\boldsymbol{\phi_W}$) from interferograms in Figure 3.

Expression (7) gives a phase value wrapped in the range from $-\pi$ to $\pi$ (hence the origin of its name), so that an unwrapping process is necessary to eliminate discontinuities (generated by the $\tan^{-1}$ function) not present in the actual measurement, and thus estimate a continuous phase (unwrapped phase) [21]. Figure 5 is the unwrapped phase ($\hat{\phi}$) from Figure 4.

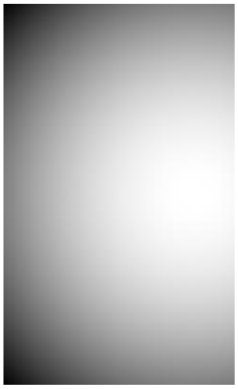

**Figure 5.** Unwrapped phase ($\boldsymbol{\hat{\phi}}$) from Figure 4.

## *II.III. Optical microscopy*

In order to study very small objects, it is necessary to use instruments that allow to magnify their image. It is possible to use a simple magnifying glass or, if a very large magnification is desired, a compound microscope; where the focal length of the instrument is very short [15,17]. Taking care that aberrations are not too large, the magnification of a simple magnifier is limited from 3X to 20X [15]. On the other hand, speaking of compound microscopes, the lens that achieves the high magnifications is called “objective” and is the lens closest to the specimen [15]. One way to classify objectives is according to the medium that exists between them and the specimen to be analyzed; being dry or immersion. The parameter that defines the objective resolving power is the Numerical Aperture (NA), which is the light collecting capacity and can be increased by approximating the medium refractive index ($n$) at the objective exit with the objective index. This parameter is given as

$$\mathrm{NA} = n\sin(\alpha) \tag{8}$$

where $\alpha$ is the angle formed between the optical axis and the marginal beam [15,17,19,26]. Figure 6 presents an oil immersion objective, where on the left side there is a substrate-oil interface at the objective exit, while, on the right side of the figure, there is an air gap. In this figure, the optical axis is shown as a dash-dotted line. Talking about the marginal rays coming from the sample, on the left side the marginal ray (dashed line) is collected by the objective, but on the right side the marginal ray (dotted line) is missed; all of the aforementioned happens due to the refraction of rays depending on if there is a mismatch in the refractive indices or not.

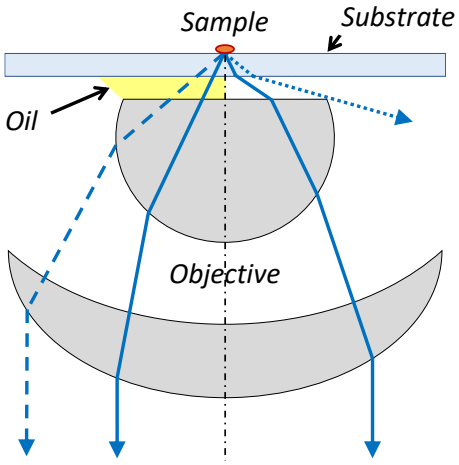


**Figure 6.** Role of immersion oil on a large numerical aperture microscope objective. In this representation, the dash-dotted line is the optical axis, the dashed line is the marginal ray collected by the objective and the dotted line is the missed marginal ray.

There are multiple types of microscopes with particular optical configurations that offer considerable advantages. To select the most adequate microscope to work, it is necessary to consider the type of specimen and the parameter to be studied [26].

## *II.IV. Optical trap*

In 1970, Arthur Ashkin reported particle trapping using the radiation pressure force of a continuous laser [1]. That force is due to the exchange of linear momentum between the electromagnetic radiation and the object (particle). This can occur by absorption or reflection of light on the particle, regardless of the wavelength used [27]. As an example of application, in imaging soft structures, radiation pressure (whose stiffness is in the range of $10^{-3}$ to 1 pN $nm^{-1}$) could be an alternative to atomic force microscope (AFM) cantilever which has a stiffness from 10 to 105 pN $nm^{-1}$ [28]. Then, radiation pressure ($P_{rad}$), at normal incidence, is determined by the expression

$$P_{rad} = \frac{I(R+1)}{c},$$

(9)

where $I$ is the irradiance, $R$ represents the surface reflection coefficient, and $c$ is the speed of light [27]. With an unfocused Gaussian beam (Figure 7a), the momentum generated by the refraction holds the particle at the beam center, where the gradient is balanced, and it can be pushed in the direction of beam propagation by the radiation pressure [3]. On the other hand, when the beam emitted by a laser is focused by a lens (Figure 7b), the pressure at the beam waist will be higher than in the rest of its optical path, the transversal gradient increases and a new axial gradient is generated, adding to the beam scattering force [2,3,13,29]. This makes it possible to keep a micrometer or sub-micrometer scale particle trapped in the beam waist, which gives it the name optical trap. The use of different laser power levels for optical traps has been reported in the literature, ranging from a few mW to 1 Watt or more in the specimen plane, depending on details of the laser and setup, objective transmittance, and the desired stiffness [2]. In Figure 7, red arrows represent the main scattering forces, which pointing in the beam propagation direction, and gradient forces are depicted by green arrows, which are perpendicular to the scattering forces [2].

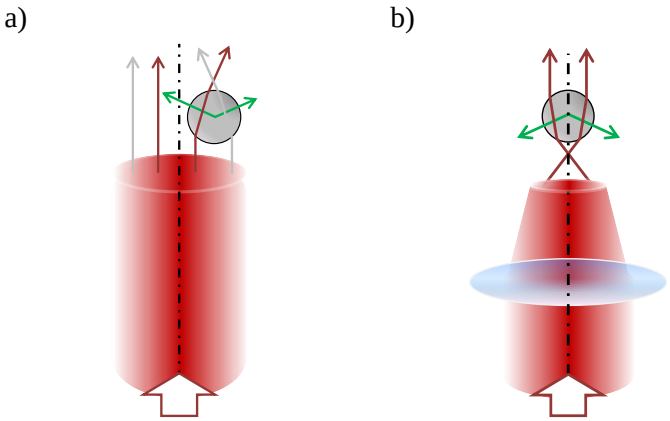


**Figure 7.** Ray optics description of the gradient and scattering forces. The red arrows represent the main scattering forces, the gray arrows are the secondary scattering forces and gradient forces are depicted by green arrows. a) Unfocused beam and b) Focused beam by a lens.

Depending on the particle size and the wavelength used, the criteria explaining the optical trap operation will be determined. If the particle is bigger than the wavelength, Mie scattering theory (ray tracing) is used (Figure 8a); in these case, refraction of the incident light by the particle corresponds to a change in the momentum carried by the light. Otherwise, if the particle is smaller than the wavelength, Rayleigh scattering theory is used, where a single electric dipole positioned at the center of the particle can be considered (Figure 8b); in these case the forces (scattering and gradient) are calculated electromagnetically [2,3,29–31]. Given the characteristics of our experiments, Mie's theory will be used.

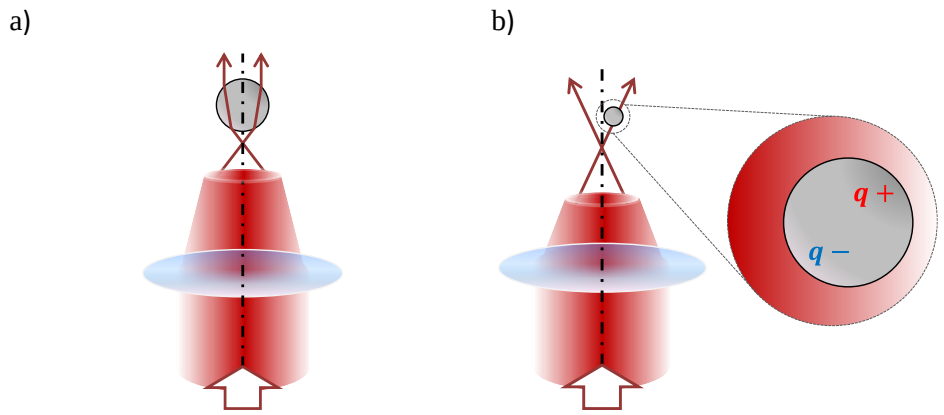


**Figure 8.** Representation of trapping regimes: a) Mie, b) Rayleigh. The red arrows represent the main scattering forces.

To generate an efficient optical trap requires that the beam focused by the lens come from a large NA, so it is necessary to use an immersion microscope objective (100X y NA≈1.3). Although oil is commonly used as the immersion medium, there are also experiments using water immersion objectives [32]; the experimental conditions determine whether one or the other is chosen [33]. However, many radiation pressure studies neglect the immersion media optical contributions used for their implementation [34–37], often due to their transparent nature or simply because such media are a constant in any optical trap. Common immersion media, such as water or oil, have effects of the same type but on a different scale, so their contributions are a factor to consider in work using immersion objectives where trap geometry is of interest or where interferometric quantifications are performed through phase recovery [37,38]. Regarding the influence of an immersion medium in an optical trap, it has previously been reported how the optical excitation of oil can influence the change in the trap focal length [39], and the same effect has been proven by testing immersion oils of different refractive indices [40]. It has also been reported that by combining a confocal microscope and an optical trap, when using independent laser sources that share the same immersion objective, the change in the optical trap laser power changes the confocal focus position [41,42]. The variation in the beam convergence geometry has been considered as an effect on fluid pressure [43], as well as a change in the quantum state of the matter and radiation [44], and even the thermal effects of this convergence that are induced by modulation in radiation power have been characterized [45]. The contributions induced by laser radiation on system components will be discussed here.

On the other hand, the most common applications of optical tweezers are in biology [29,46,47] and in the micromanipulation of other types of particles [47,48]. Over the years, optical traps have been combined with various non-invasive measurement techniques [36], such as the holographic optical tweezers [49–51] or optical trap spectroscopy [52]. Biological characterizations have even been carried out with optical tweezers and interferometric techniques [53].

# III.

# Optical Trap - Mach-Zehnder Interferometer Setup

# *III.I. Integration of Optical Trap and Interferometer*

## III.I.I. Optical trap setup

The optical trap system used (see scheme in Figure 9) consists of a THORLABS™ butterfly laser diode type infrared (IR) laser source (model BL976-SAG300, with a wavelength ($\lambda_{IR}$) of 976 nm and a maximum power of 350 mW) and an oil immersion microscope objective (Nikon brand, model MRP71900, with 100X magnification, NA=1.25 and a working distance (WD) of 0.23 mm); MO2. The immersion oil (Non-Drying Immersion Oil for Microscopy, Cargille Type LDF [54]) has a refractive index ($n$) of 1.5181. The substrate shown in Figure 9 is a PEARL coverslip (used as a slide) of 24 x 50 x 0.13 mm in dimensions and with a refractive index of 1.52. Therefore, the maximum distance available for particle trapping is approximately 100 µm, which means that to keep the optical trap above the slide, the immersion oil must not exceed approximately 100 µm in thickness; this is controlled by moving the slide along the trap optical axis. The specimen slide is placed on a 3-Axis NanoMax™ stage (model MAX311D), where the fine adjuster can move up to 300 µm. To observe the sample under study, it is illuminated by a white LED light source through a condenser lens (MO1) in the opposite direction to the IR laser.

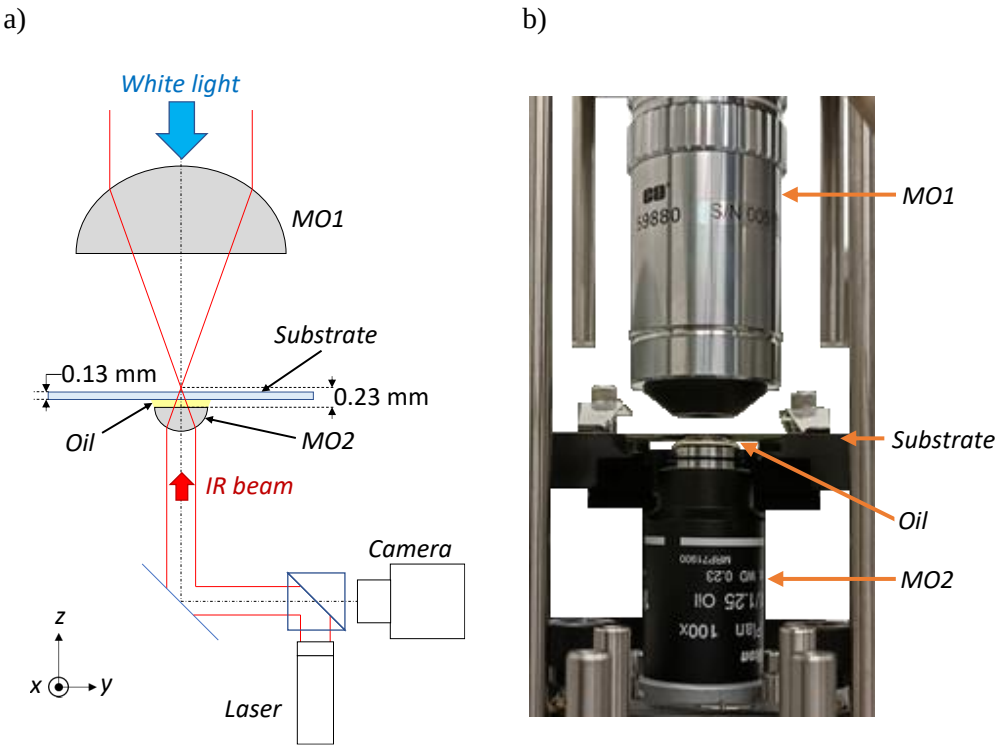


**Figure 9.** Representation of the usual operation of an optical trap. (MO1—Condenser Microscope Objective, MO2—Oil Immersion Microscope Objective). a) Scheme, b) Experimental setup. In this setup, laser is redirected (by a dichroic beam splitter and a mirror) to MO2, which focuses the beam and forms the optical trap, then the beam continues its optical path, although it is no longer of interest for the experiment. Apart from that, white light is captured by MO1, illuminates the working area and continues its trajectory to form image in camera.

## III.I.II. Interferometer setup

A Mach-Zehnder interferometer was integrated into the optical trap system. The experimental setup corresponding to the interferometer used is shown in Figure 10. The interferometer light source is a KIMMON KOHA laser (model KBL-100-A) with a wavelength ($\lambda_B$) of 405 nm and a maximum power of 100 mW; in this laser, the coherence length decreases below 300 µm when a power lower than 1 mW is selected [13], and this makes it possible to obtain interferograms that are free from spurious interference, and also to perform non-invasive measurements (without affecting the object under study).

The laser beam passes through a beam expander system and is incident on a 50:50 dichroic beam splitter. The reflected part, the reference arm, is incident on a mirror that is attached to a piezoelectric (PZT), which is controlled by a THORLABS variable voltage source (model TDC001), in order to apply the phase shifting technique in the interferogram demodulation; then, continuing on its path, the wavefront is redirected to a second beam splitter, also 50:50. On the other hand, the part transmitted by the beam splitter at the laser output, passes through Microscope Objective 1, MO1 (Edmund brand, model 59880, of 100X with an NA of 0.8 and a WD of 3 mm), and then, after going through the sample under study, light is captured by a second microscope objective (MO2), to be redirected by a mirror, until it crosses the second beam splitter. Here is where the beams recombine and interference is generated.

The image capturing video system consists of a THORLABS camera (model DCC1240c) based on a CMOS sensor with a pixel size of 5.3 µm and a resolution of 1280 x 1024 pixels. The field of view generated between Microscope Objective 2 and the camera is 61.24 x 48.99 µm.

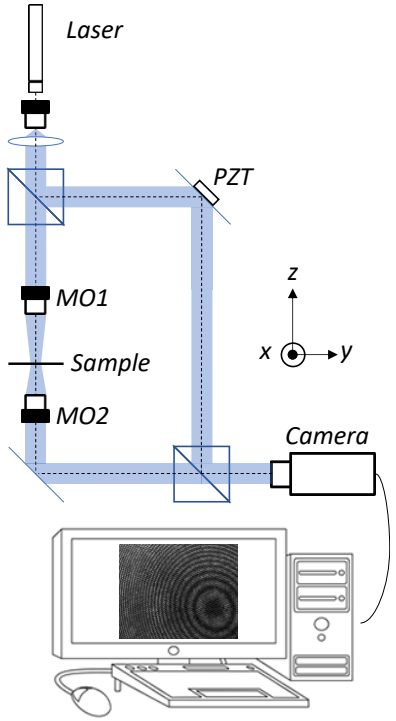


**Figure 10.** Scheme of the Mach-Zehnder interferometer used. (MO1— Long Working Distance Microscope Objective, MO2—Oil Immersion Microscope Objective).

With the system described above, it is possible to obtain interference patterns such as the one shown in Figure 11, whose capture was performed with the LabVIEW™ program, while image processing was carried out with the MATLAB™ programming language. Figure 11 shows the interference fringes, the intersection of the red lines indicates the center of the camera field of view and the yellow circle represents the optical trap position.

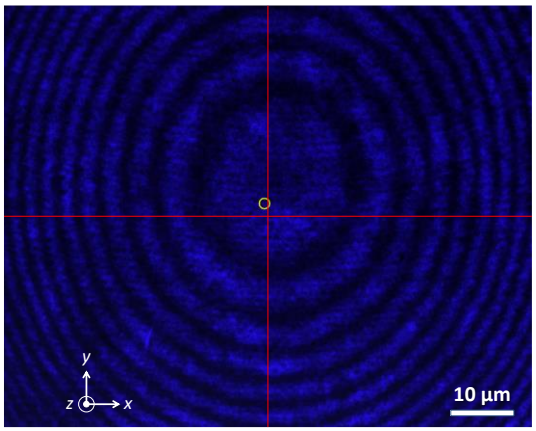


**Figure 11.** System alignment. The intersection of the red lines indicates the center of the camera field of view and the yellow circle represents the optical trap position.

The phase difference $(\Delta\phi)$ between the two interfered wavefronts, previously mentioned, is given by [19]

$$\Delta\phi(x,y) = \frac{2\pi}{\lambda}\mathrm{OPD}(x,y), \tag{10}$$

where $\lambda$ is the wavelength and OPD is the optical path difference.

For each point $p$ in $(x,y)$ on the screen where the interference pattern is projected (in this case, each pixel of the CMOS sensor), the difference in the trajectories traveled is different, but directly related, according to

$$h(x,y) \times \Delta n = M(x,y)\lambda = \frac{\phi(x,y)\lambda}{2\pi}, \tag{11}$$

where $h$ is the thickness of the object under study (through which the object beam was transmitted), $\Delta n$ is the difference of the refractive index with respect to the reference beam, and $M$ refers to the fringe order, which is proportional to the phase difference. This expression is derived from Eq. (5).

## III.I.III. Integrated systems

Figure 12 corresponds to the setup resulting from the integration of the optical trap with the Mach-Zehnder interferometer, previously explained. Based on the optical trap setup, the blue laser replaces the white light source, while the condenser objective is replaced by the long working distance objective. Before the blue laser enters this objective, the expander and the first beam splitter are placed, and finally, the reference beam is redirected to the splitter in front of the camera; it should be noted that the low numerical aperture of the long working distance objective, together with the low power of the blue laser, does not allow the generation of a significant gradient force that would disturb the optical trap. The rest of the optical trap system remains unchanged; so, both configurations share the large numerical aperture microscope objective (MO2) and, consequently, the same immersion oil.

In this way, the interaction of the optical trap with the structures under study can be quantitatively analyzed by the integrated Mach-Zehnder interferometer. Yet, if the power of either laser source changes, the interferometric measurements will have an additive phase effect that must be compensated for.

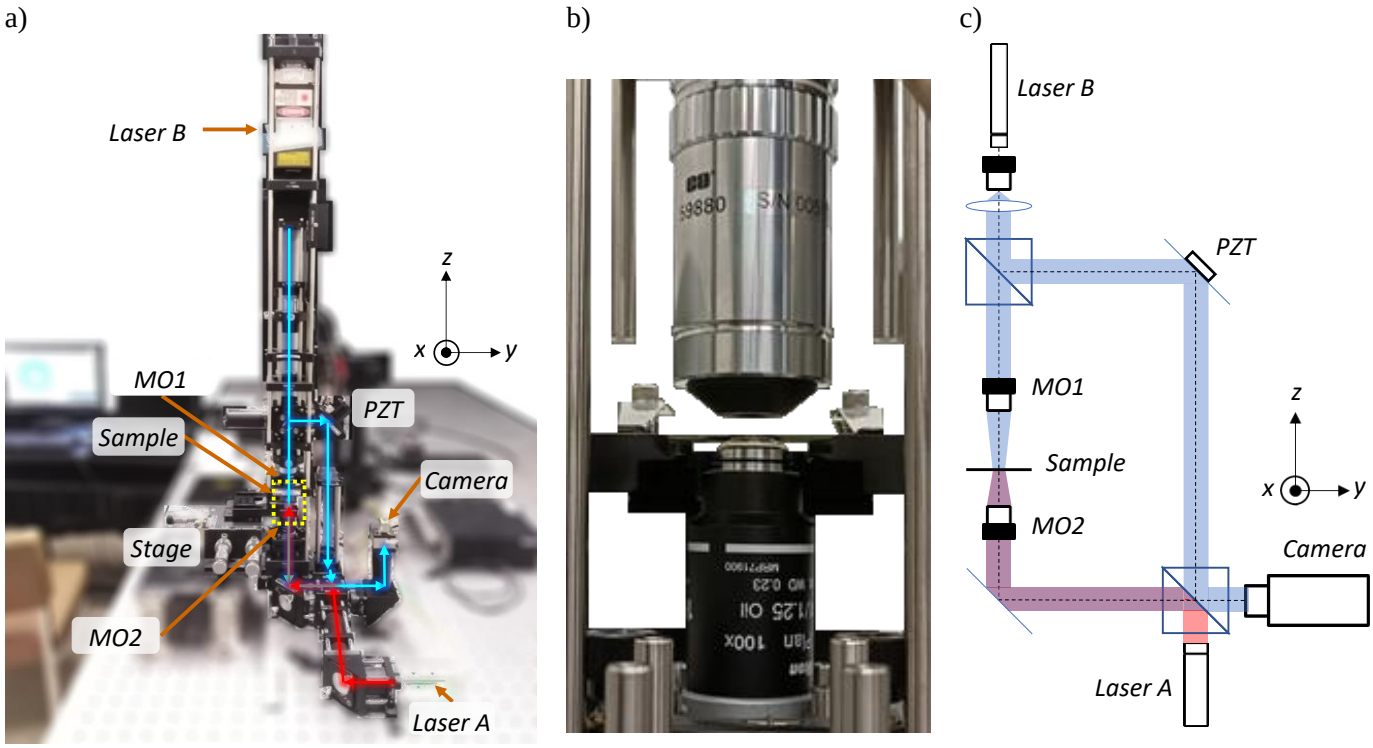


**Figure 12.** Optical Trap - Mach-Zehnder interferometer setup. a) Experimental setup, b) Zoom where the Optical Trap is formed (region inside the yellow dotted line square in a)) and c) Scheme. (MO1—Long Working Distance Microscope Objective, MO2— Oil Immersion Microscope Objective).

# *IV.*

# *Evaluation of Effect per Individual Media*

In previous experiments, using the interferometer-trap configuration, it was noted how, as the optical trap trapping force increased or decreased, the interferograms exhibited a phase shifting directly proportional to the change in laser output power. The same effect, although with a different ratio, was observed when keeping the trapping force constant and now changing the interferometer laser power. Since in both cases, the phase shifting was directly proportional to the change of power, and since the direction of propagation of both lasers is opposite to each other, then a mechanical effect caused by the radiation pressure could be discarded as the cause of the phase addition; otherwise, the phase shifting for some of the sources should be inversely proportional to the change in power. Thus, the cause of the above effect must be in one or some of the optical elements on the object arm that the optical trap and the interferometer share. To identify these elements and their contribution to the phase addition effect, the following experiments are proposed; they include independent external analyses for the elements located around the optical trap.

## *IV.I. Identification of optical elements contributing to phase shifting*

Considering the study published in [42], in which a variation in the confocal microscope optical geometry as a function of IR laser radiation is reported, the first experiment of the manuscript presented here aimed to study the optical trap position with respect to the optical element in which it is formed (no trapped particle), i.e., the relative trap position was changed moving the substrate, from the sample immersion medium (located above the slide) down to the immersion oil, going through the slide. It is important to remember that the change of trap position is possible because the sample is placed on a 3-axis stage with micrometer accuracy. Considering the stage limitations, it was decided to perform this analysis starting when the trap is formed at 50 μm above the substrate (air), while 0 indicates the point where the trap is formed at the air-glass interface. At each height interval, the IR laser power was changed, evaluating the power required for the phase addition to correspond to a value of $2\pi$ radians. Since power is directly proportional to intensity (Power = Intensity × Area), it follows that the intensity-phase ratio is also linear. Experimentally, the laser power can be manipulated, so this variable is used in this work.

If the ratio power-phase were to remain constant in the different media, then no medium responsible for generating the additive phase could be identified. However, the results presented in the graph in Figure 13 provide evidence that by placing the trap in the immersion oil, the phase addition is more sensitive to the change in power when compared to the slide glass and the medium in which a sample would be immersed over the slide, which in this case was air. It is observed how less power is required to cause a phase shifting of $2\pi$ when the trap is placed in the oil (between −130 and −240 μm, with respect to the substrate top face).

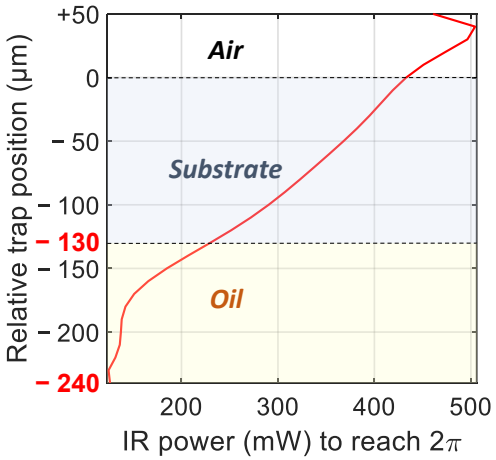


**Figure 13.** IR power required to cause a $2\pi$ shift depending on trap position.

Quantitatively, interference patterns were taken from 0 to 300 mW in 5 mW intervals, then was calculated the absolute value of the subtraction of each interferogram with the reference (0 mW) and finally, as there is a matrix of values, rows and columns were averaged at one point. For example, Figure 14 plots (in blue points) the average subtraction between interferograms when the trap is located at −240 μm with respect to the substrate top face. It is observed in the first powers in the graph that subtraction is not very smooth (probably due to environmental disturbances), but as the power increases, so does the phase difference. However, since phase is periodic, the phase difference will also adopt this property. This is useful to identify the amount of power required to cause a complete phase shifting ($2\pi$) in interferograms. Following the red dotted line in Figure 14, it can be seen that, at this position, the IR laser takes ~135 mW to generate a shift of $2\pi$ in the interference fringes.

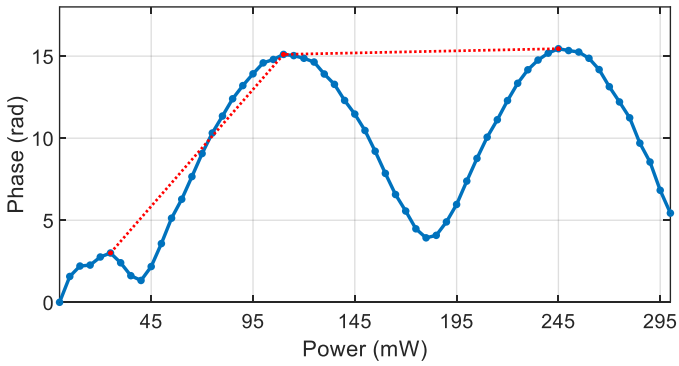


**Figure 14.** IR power required to cause a $2\pi$ shift with the trap located at −240 μm. The blue points indicate the average subtraction between interferograms with phase shifting and a reference. The red points indicate a maximum peak.

To corroborate the major contribution of oil to the detected phase shifting, independent tests of oil, water, air and glass were conducted at the macroscopic scale outside the optical trap. Since in the trap-interferometer setup it is not possible to measure variables separately, three systems were designed. In order to study the refractive index, another Mach-Zehnder interferometer was mounted

and the element was contained; to measure the temperature, a thermocouple was used; to characterize the topography, and then calculate the volume, a Michelson interferometer was used. In the subsequent sections, the optical, thermal and volumetric analysis experiments of these elements, particularly oil, are described. Thus, by knowing the contributions of each material, it will be possible to calibrate and correct measurements.

## IV.I.I. Refractive index test

The experiment proposed above makes it possible to identify that there is a different phase contribution from each element, but it does not make it possible to determine the contribution of each of these or whether only one of them contributes. Therefore, an experiment (Figure 15) was performed by assembling a Mach-Zehnder interferometer, outside the optical trap system to test each element separately on a macro scale (air, glass, distilled water and oil), while they are excited with a second laser beam (different from the interferometer). The interferometer has a He-Ne laser source with a $\lambda$ of 633 nm ($\lambda_{Pr}$) and a power of 12 mW. The beam is spatially expanded and filtered. In addition, it has two non-polarized 50:50 beam splitters. On the observation plane is a PIXELINK camera (model PL-B741F) with a CMOS sensor, 6.7 μm pixel size (1.3 Mpx) and 1280 x 1024 pixels resolution. The camera sensor was exposed without having a lens attached.

The laser used to excite the elements of interest is a SPECTRA-PHYSICS solid state laser (model Excelsior-532-100) with a $\lambda_{Ex}$ of 532 nm and a fixed power of 100 mW; the beam diameter that is obliquely incident (45°) on the sample is 0.7 mm. This angle of incidence was determined due to the setup geometry; which is not critical in the results. Although it would have been possible to excite on-axis with the excitation laser, in order to prevent the exposed beam from hitting the camera sensor and saturating or damaging it, it was necessary to illuminate obliquely, resulting in that angle.

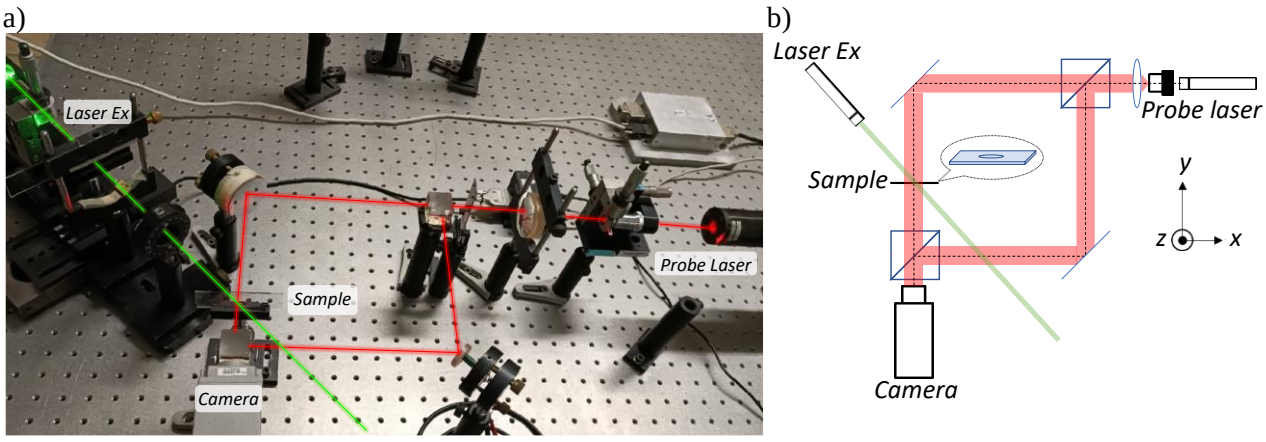


**Figure 15.** Mach-Zehnder interferometer used to study refractive indices: a) Experimental setup photo, b) Scheme.

A wide variety of slide types are available for various applications, for example, for flow applications [55]. In this work, to study glass, water and oil, an optical container was fabricated consisting of a 1.1 mm thick glass slide with a central perforation of 10 mm in diameter. A coverslip was placed on each

side of the slide; one was fixed with optical adhesive and the other was attached only through atomic interaction with each element in question.

To characterize air, the container was completely removed. For the glass analysis, a regular slide was placed, without perforation. For distilled water, the container filled with this liquid was positioned in the area of interest, and the experiment was carried out in a similar fashion with the immersion oil.

Figure 16 shows the changes in the refractive index of the four analyzed media after 20 s of excitation with the green laser. These results allow us to identify oil as the element that makes the greatest contribution to the additive phase to be removed from the measurements made with the optical trap and Mach-Zehnder interferometer system. In both air and glass, only problems of interferogram detuning are observed, without any contribution from the excitation of those elements. However, the change in the refractive index of distilled water and immersion oil is easily observed; specifically, taking the difference between the maximum and minimum values for each figure, Figure 16c ($5.47\text{x}10^{-6}$) and Figure 16d ($4.47\text{x}10^{-5}$), the change in oil is 8.17 times higher than that of water.

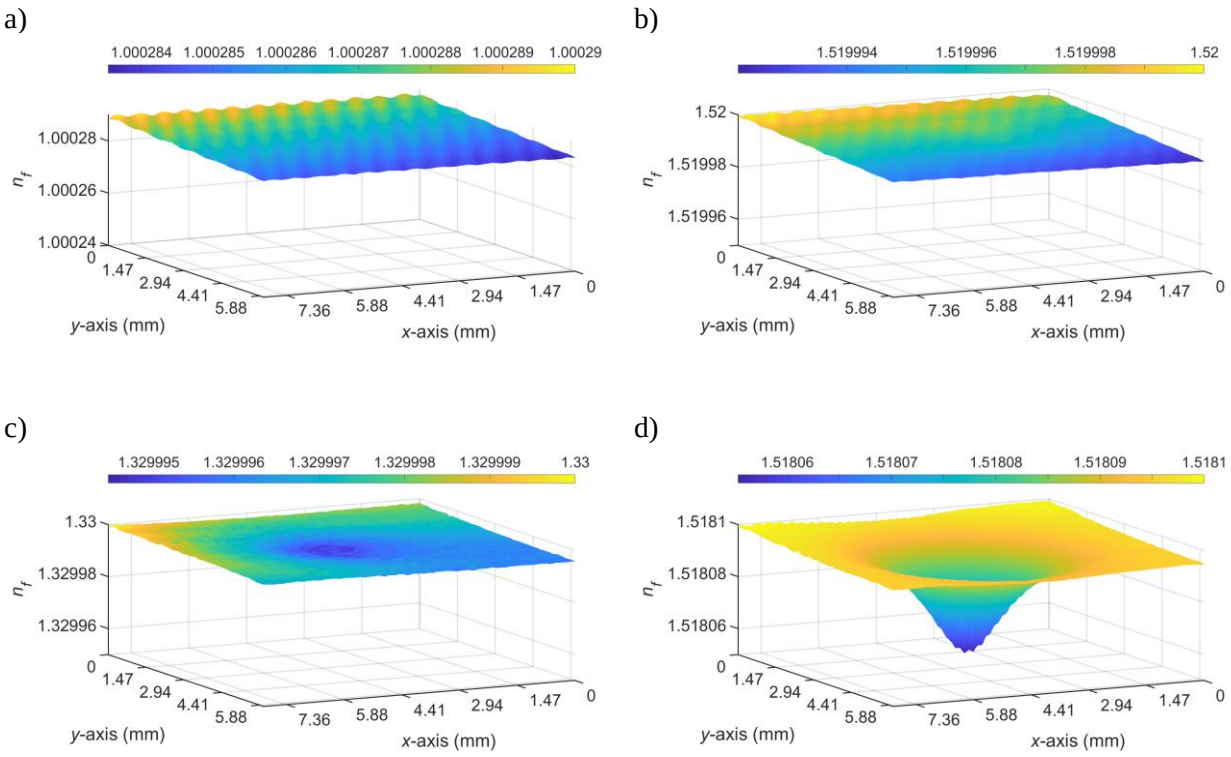


**Figure 16.** Refractive index change when laser radiation excites: a) Air, b) Glass, c) Distilled water, d) Immersion oil.

The refractive index changes shown in Figure 16 were calculated from the phase recovered from the interferograms corresponding to each element by the expression

$$n_f = n_i - \left(\frac{\phi}{2\pi}\frac{\lambda_{Pr}}{h}\right), \tag{12}$$

where $n_f$ is the medium refractive index when it responds to the excitation laser, $n_i$ is the unexcited medium refractive index, and $h$ is the sample thickness; this last parameter was kept constant for each medium (1.1 mm).

It is now possible to evaluate, to a first approximation, how much the trap position (the immersion objective working distance, WD) would change if the trap were totally immersed in the oil and the refractive index change were to change uniformly throughout the oil, using the equation

$$\mathrm{WD} = \frac{d}{\tan\left(\sin^{-1}\left(\frac{\mathrm{NA}}{n}\right)\right)}, \tag{13}$$

being $d$ the distance from the optical axis to the marginal beam at the output of MO2. Figure 17 plots the behavior between the change in refractive index (*x*-axis) and the corresponding change in working distance (*y*-axis), which is equivalent to the change in trap position [39] or to the focus position in a confocal microscope [42].

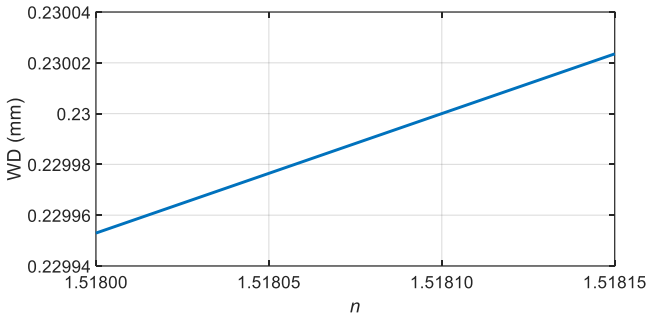


**Figure 17.** Behavior of the refractive index of the immersion oil and the working distance of an oil immersion objective.

In addition, Liu reports that the higher the objective NA, the less power is required for a given ΔWD. It is agreed that, as the laser power is increased, the WD decreases; furthermore, the trap gradient force is higher, the oil is excited, and the oil's $n$ decreases [39].

## IV.I.II. Temperature test

The purpose of this experiment is to isolate the temperature measurements from other variables, so thermal analysis of immersion oil was performed by exciting it with the same laser as in the previous experiment ($\lambda_{Ex} = 532$ nm), and measuring the temperature with a low-cost type K thermocouple, whose sensor is 1.15 mm in diameter. Although this thermocouple is relatively big, our laboratory technical limitations force us to use it. Figure 18 shows the experimental configuration set up for this purpose, where the laser is observed being incident in a normal orientation in the container center. Unlike optical metrology techniques that are usually full-field and do not require direct contact with the sample, the thermocouple must be immersed in the oil to make not only a local

measurement of temperature, but also that of the surrounding oil. Therefore, when the thermocouple is immersed in the oil, it can be directly excited by the laser beam, mixing its own temperature with that of the oil, which would generate incorrect measurements.

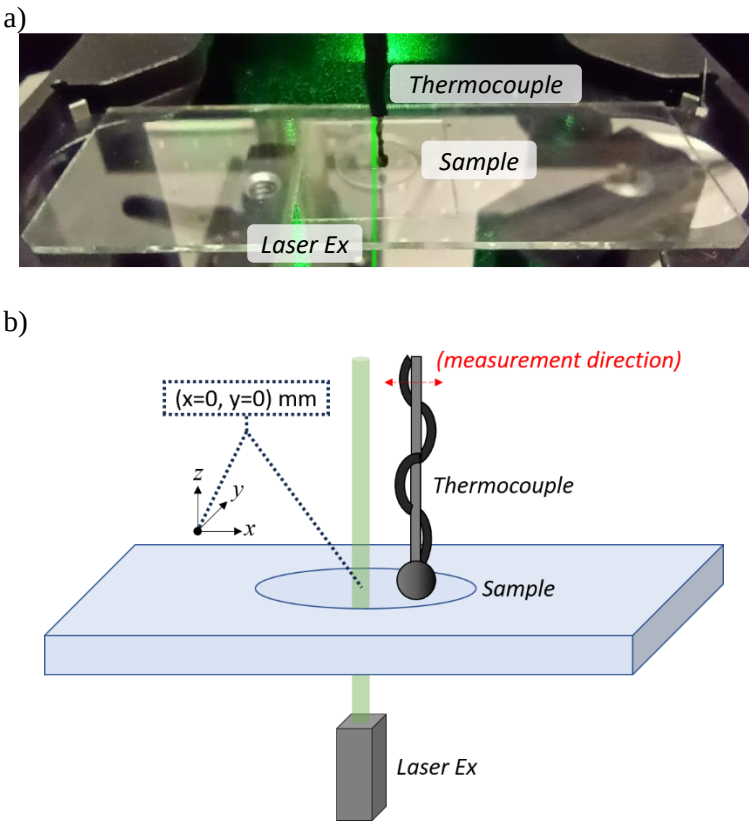


**Figure 18.** Experimental setup used to analyze thermal behavior: a) Photo, b) Scheme.

To prevent that problem, the thermocouple was positioned as close as possible to the laser beam, but avoiding direct excitation. To find this position, an oil-free container was used, and the thermocouple was placed at the *x*-axis negative end (with $y = 0$ mm), at a *z*-height of just a few microns above the container bottom. From this point, air temperature measurements were made along the *x*-axis, passing through the laser beam center incident on the $x = 0$ mm, $y = 0$ mm position. The experiment was then repeated with the container filled with the immersion oil. The limitations of this setup are the mechanical mount resolution that positions the thermocouple, thermocouple size, thermocouple sensitivity and container diameter, which allowed a small amount of data to be collected, but with good repeatability. The results of air temperature (taken as a reference) and oil are presented in Figure 19, where it can be observed, in the profile corresponding to air, that the position closest to the laser where the thermocouple receives minimum excitation is $x = -0.5$ mm, $y = 0$ mm. Figure 19 also shows that the thermocouple starts to behave erratically the closer it gets to the laser beam center, where the points correspond to valid measurements and the crosses are erratic measurements. It is important to note that the temperature distribution is not symmetrical because the thermocouple geometry is not

symmetrical; the manufacture and use of the thermocouple affects its symmetry, which affects its measurements.

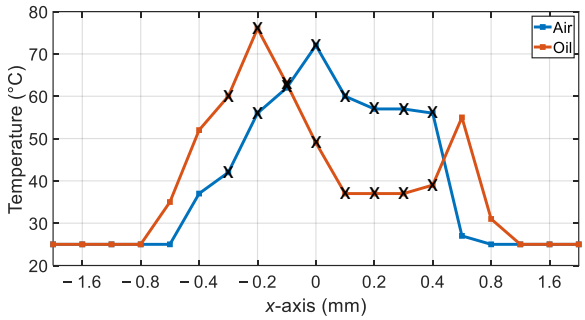


**Figure 19.** Air and oil temperature profiles. Crossed-out readings indicate erratic thermocouple behavior.

To directly distinguish the contribution of the heated medium of interest (immersion oil), the temperature difference between air (empty container) and oil was made. The profile for the temperature differences is shown in Figure 20. If above-mentioned erratic measurements, in this case between −0.3 and 0.4 mm, are discarded, it is possible to calculate -with MATLAB™ fit function- an approximate temperature profile that corrects thermocouple behavior (red line in Figure 20), and which is congruent (similar in shape but reverse in direction) to the refractive index change map central profile in Figure 16d. Thus, it can be inferred that oil reaches a temperature of around 120 °C at the beam center.

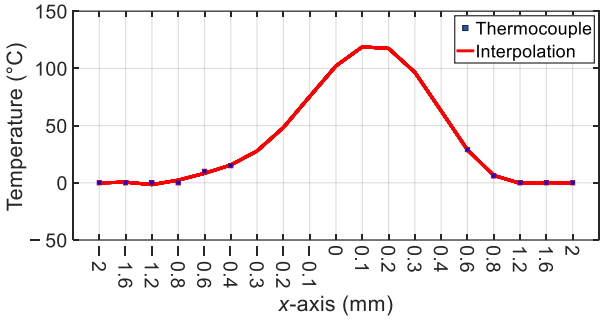


**Figure 20.** Oil temperature profile vs thermocouple position. Values showed as crossed out in Figure 19, here were removed and replaced for the interpolation curve.

Positioning the thermocouple at $x = -0.5$ mm, $y = 0$ mm, a temporal analysis of the oil temperature was then performed. In that experiment, measurements were taken under three different conditions: first with the laser source off for 10 s, then in a second scenario of 20 s with the laser on, and finally, a third scenario of 20 s with the laser off again; in all of them, measurements were taken continuously at 1 s intervals. The same procedure was applied in the experiment of section IV.I.I where the refractive index change was measured, although in that section, only the result for the 20$^{th}$ second of the second scenario, which corresponds to the maximum excitation time, was presented.

Figure 21 plots the thermocouple measurements as a function of time, and compares them with the optical phase map maximum value corresponding to the refractive index. It is observed that in both cases, the oil gets excited and relaxes at approximately the same time intervals, whereas in this case, the thermocouple is slower to react to the change. It is important to mention that the oil returns to its initial temperature and refractive index in less than 20 s.

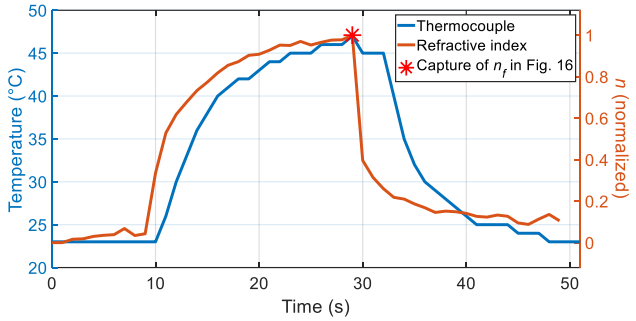


**Figure 21.** Comparison of thermal behavior and refractive index of oil over time. The asterisk indicates the point that was analyzed in Figure 16.

## IV.I.III. Volumetric test

To characterize the volume change caused by laser excitation, a Michelson interferometer was mounted (Figure 22), having as illumination source a THORLABS brand LED (model LED635L) that emits light with a central spectral output ($\lambda_{LED}$) of 635 nm, a half-height width (FWHM) of 15 nm, an approximate coherence depth of 25 µm, and a half viewing angle of 7°. Since the test object is the same oil-filled container, the LED's low coherence allows interference only with the first surface, where the oil is exposed and the volume change is concentrated; this way, spurious interference from other surfaces is avoided. For these experiments, the $\lambda_{Ex}$ excitation laser and the same camera that were used to analyze the refractive index were used again. In addition, the experiment sequence (without excitation, with excitation, and finally, in relaxation) was repeated. As in the temperature experiment, only the oil was analyzed.

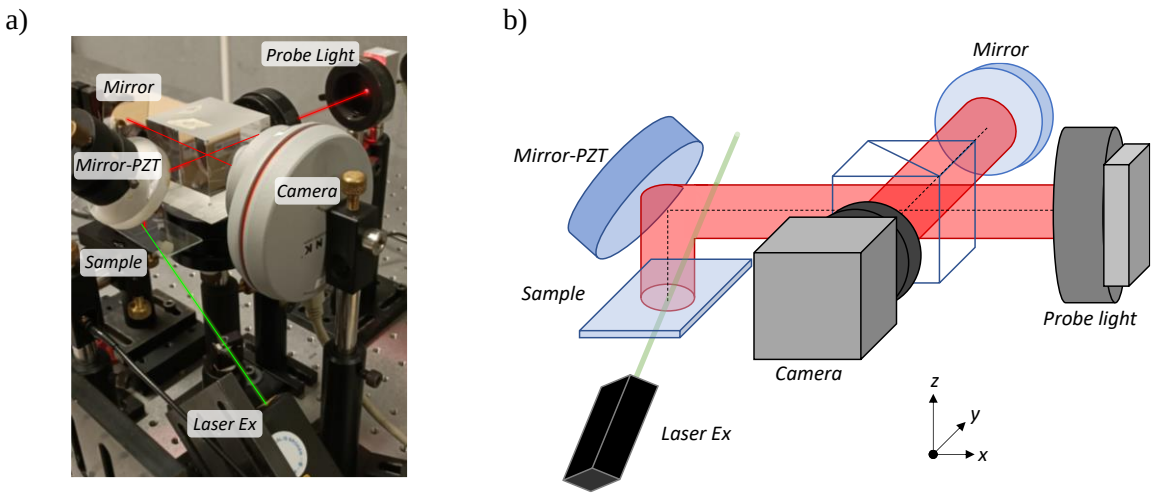


**Figure 22.** Michelson interferometer used to study volume changes: a) Experimental setup photo, b) Scheme.

In Figure 23, the change in the surface topography of the exposed oil at different times is presented. Figure 23a shows the displacement map when measured at 5 seconds, when the laser was still off; in Figure 23b, shows measurement at 10 seconds, when the laser was turned on; in Figure 23c-e represent measurements made at 15, 20 and 25 seconds, respectively; finally Figure 23f corresponds to the topography measured when the laser was off.

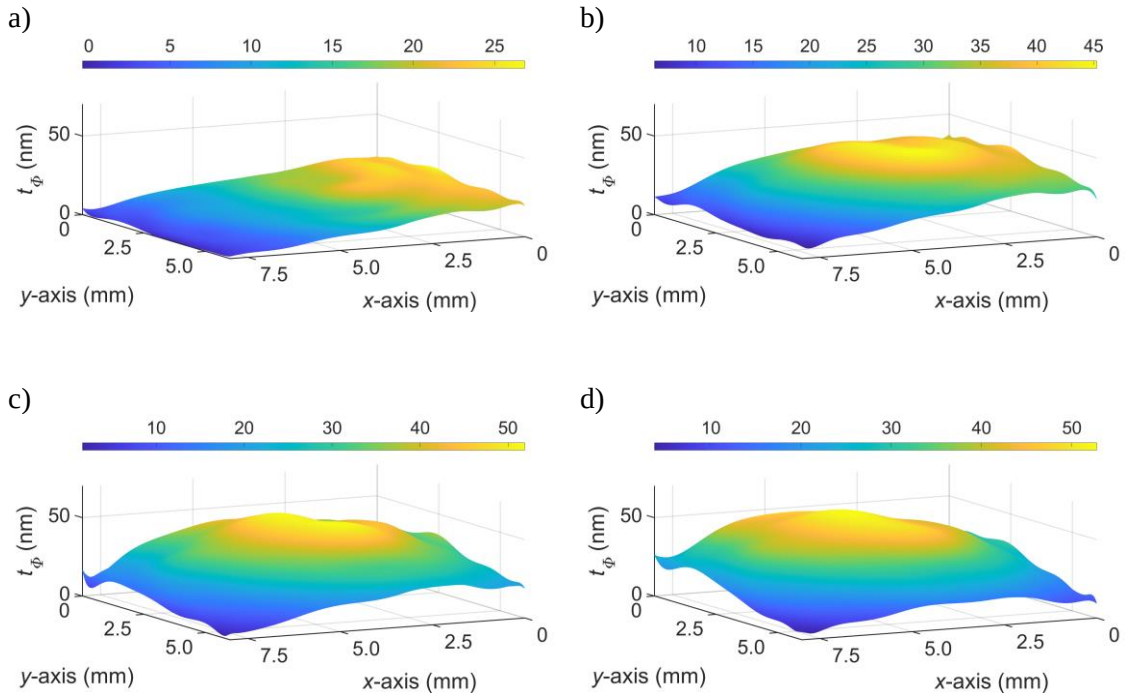

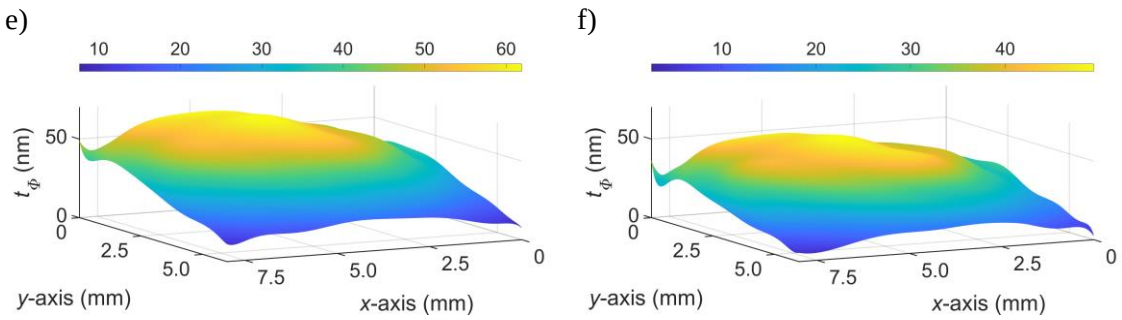


**Figure 23.** Topography changes in time when laser radiation excites at: a) 5, b) 10, c) 15, d) 20, e) 25 and f) 30 seconds.

For the Michelson interferometer used in these experiments, the topography values are obtained from the phase maps through equation

$$t_\phi = \frac{\phi \lambda_{LED}}{4\pi}, \tag{14}$$

where $t_\phi$ is the change of sample topography. This expression is derived from Eq. (4).

By integrating the volume under the surface at each point, the total volume of each measurement can be obtained with the expression

$$V = \int_0^{Ly} \int_0^{Lx} t_\phi(x, y) dx\, dy; \tag{15}$$

where $Lx$ and $Ly$ are the limits of the camera field of view, which in this case are 8 and 6 mm, respectively. Due to interferometer instability, the measurements present a detuning error; however, volume behavior corresponds adequately to laser excitation time, and can be related to the result of refractive index-temperature test, since oil expands with heat. Figure 24 shows, as a function of time, the change in volume against the change in temperature and refractive index.

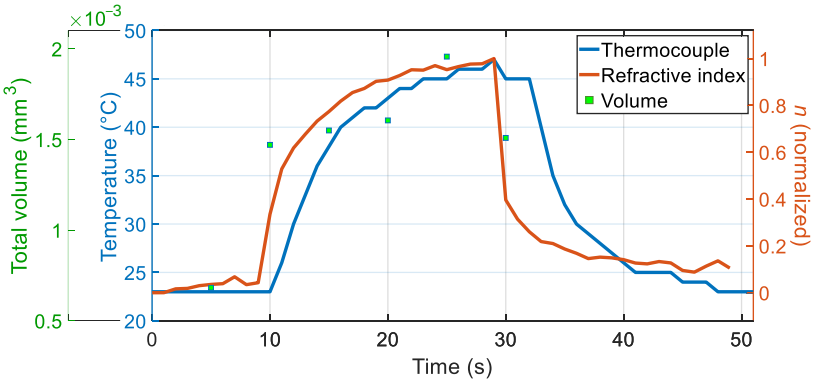


**Figure 24.** Comparison of temperature, refractive index and volume change of the oil over time.

As reported by Matrecitos-Avila, oil volume change does not represent a variable that affects her measurements due to equipment design, and therefore, she does not do that analysis [42]. However, it has been proven in this work that such change also exists and should be considered, depending on the application.

# V.

# *Calibration and Correction of the Additive Phase*

The correction procedure for an object of interest would correspond to the same procedure performed for any other test object. In this case, the simplest test object was a paint film and was only used for demonstration purposes. In this section, the correction (compensation) applied to the measurements of a black paint film made with the Mach-Zehnder interferometer integrated to the optical trap is presented. Figure 25 shows two cross-sectional images of an ink film, which was used in the experiments of this manuscript, taken with a JEOL™ scanning electron microscope (SEM) (model JSM-7800F) to measure its thickness and observe its topography.

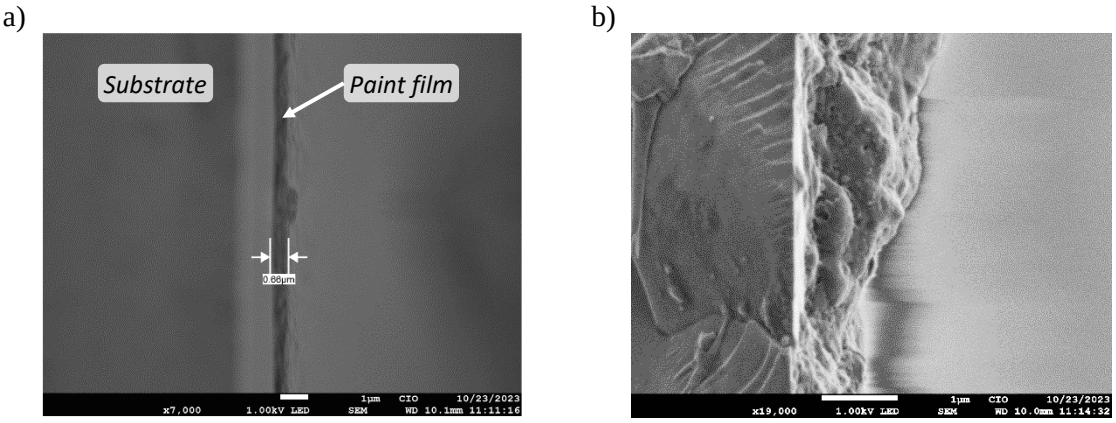


**Figure 25.** Electron microscope images of a cross-sectional view of a paint film at magnifications of: a) 7,000X and b) 19,000X.

In this case, the optical trap will generate strains and possible damage on the sample when it is exposed to different IR laser powers, while the interferometer measures the three-dimensional shape of the damage caused. That is, although in this case the optical trap works as an indenter, the strain it generates on the paint film would be of the same nature as the strain that could be measured with the interferometer on any trapped particle. It is important to note that the Chapter purpose is not to measure the damage, but the phase behavior.

## *V.I. Optical trap tests for phase calibration*

As a first approximation, calibration of the phase added by the immersion oil is performed by keeping the laser power of the interferometer ($\lambda_B$) constant, previously placing the optical trap on the upper face of the slide (glass-air interface), in an area that does not contain paint. Taking as a reference the interferogram phase when the laser that generates the trap is off (0 mW), the power of this IR laser is increased in 5 mW intervals, until reaching 300 mW, with a waiting time of 5 s between increments. In order to apply Eq. (7), five interferograms were taken at each power, with a step of $\pi/2$, and waiting 77 ms between steps; making a phase measurement in each interval, the reference phase is subtracted from each of these. The result of this experiment is shown in Figure 26, where a profile for the average of phase differences was plotted, observing that the power-phase ratio is linear and uniform throughout the phase map. Thus, knowing the increase in the trap power, it is possible to know the corresponding phase that should be subtracted from the measurements made with the interferometer, since the phase shifting could be considered spatially constant.

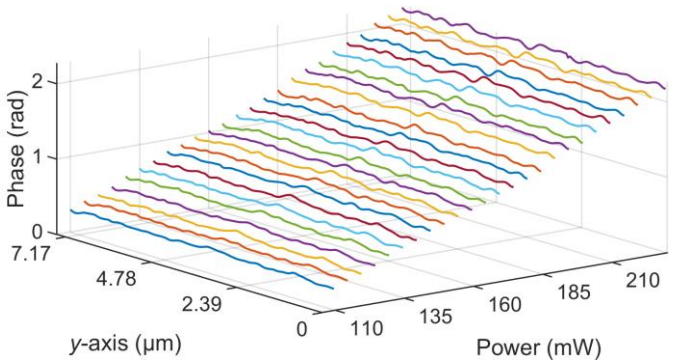


**Figure 26.** Phase shifting (in profiles) relative to power shifting from 110 to 230 mW.

However, phase distribution may not be constant throughout the field of observation; so, it is advisable to consider such effect when implementing the calibration. For example, Figure 27a shows the phase behavior when applying powers of 110, 140, 175, 205 and 230 mW, in a slide area where there is no sample (i.e. without paint). Likewise, in Figure 27b, the profiles of the gray plane in intersection with the phase maps are plotted, as they are indicated in Figure 27a. Since the behavior between phase and power is linear, only these powers were selected to facilitate visualization. In both figures, it is clear that the additive phase intervals are equispaced, although spatially variable.

a)

b)

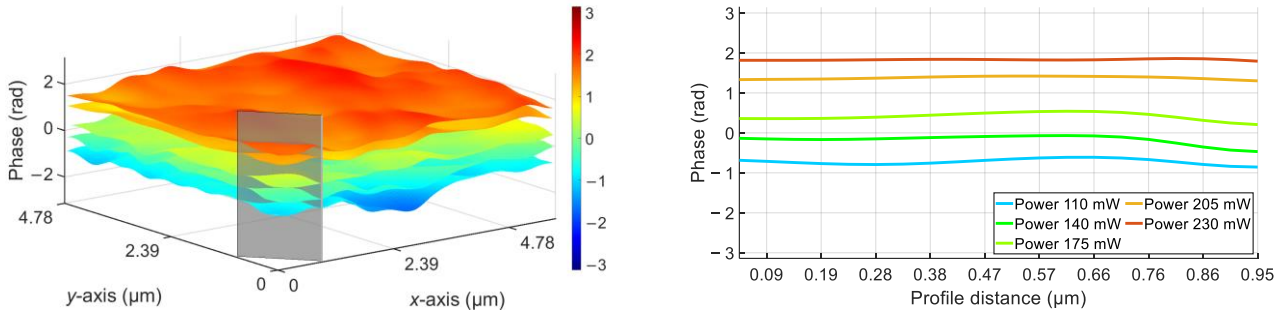


**Figure 27.** Phase piston behavior in glass using 0 mW power as reference: a) Phase mapping, b) Profiles.

Similarly, Figure 28 shows the phase values when the same powers are applied to an area of the slide where a paint sample has been deposited.

a) b)

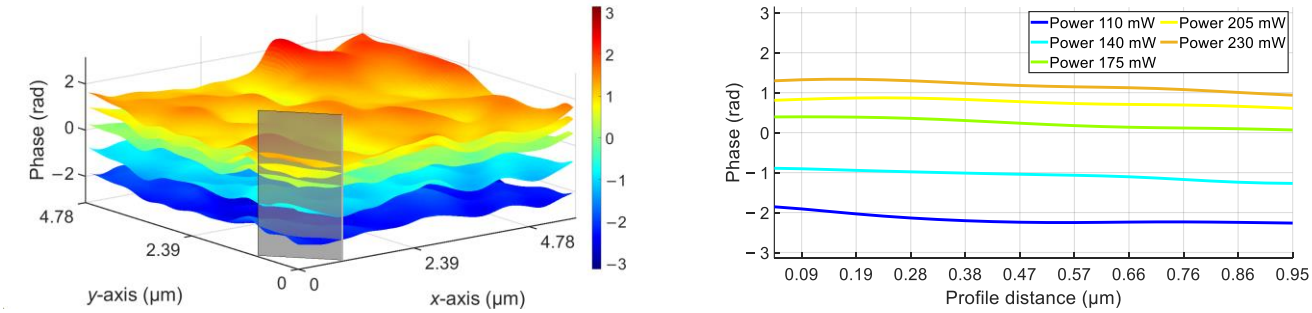


**Figure 28.** Phase piston behavior in paint using 0 mW power as reference: a) Phase mapping, b) Profiles.

In both characterizations, a positive trend is perceived, which corresponds to the phase shifting behavior in the respective interferograms. Figure 29 shows the behavior of each trend line and a sample interferogram.

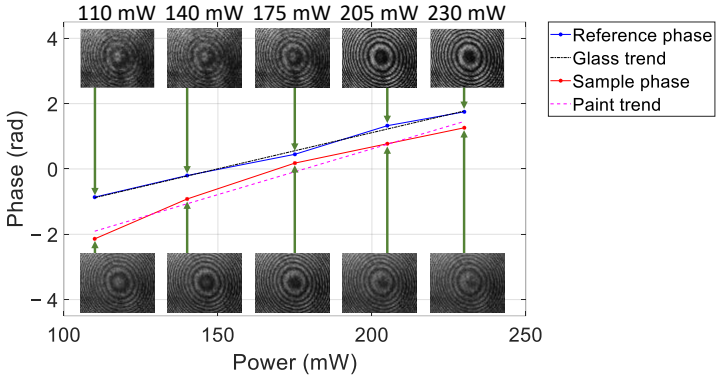


**Figure 29.** Phase shifting behavioral trend shown in interferograms as well as in phase average (point) depending on the power.

## *V.II. Additive phase correction*

It can be clearly observed how there is a piston in the phase maps in the characterization of a sample as the IR laser power is increased. Figure 30a-e present in phase the damage that the sample receives when the IR laser is positioned at the glass-air interface, and the sample is characterized at powers of 110, 140, 175, 205 and 230 mW.

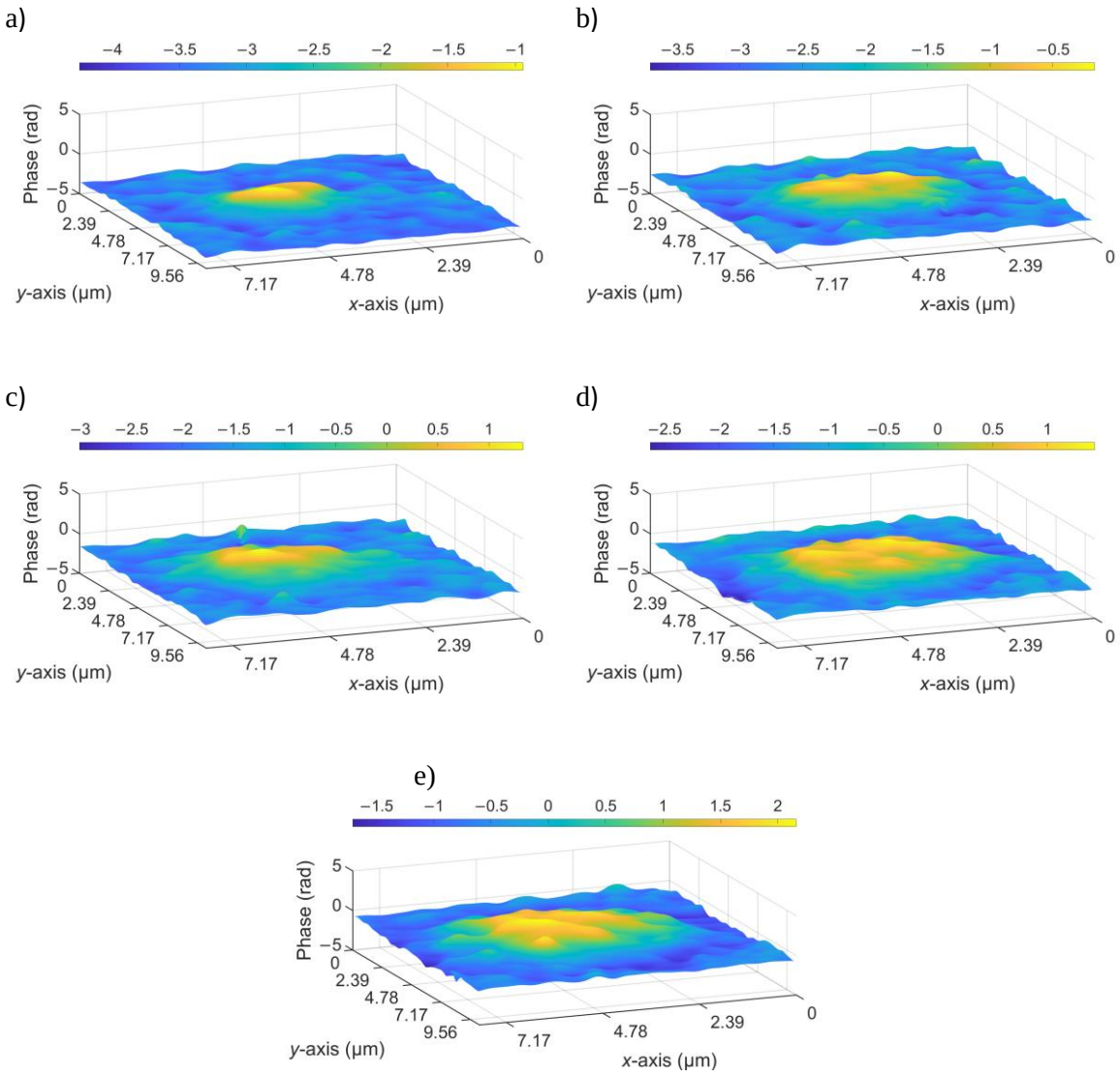


**Figure 30.** Paint damage (in phase terms) when the IR laser radiates at: a) 110; b) 140; c) 175; d) 205; and e) 230 mW. For each power, the greatest damage caused is observed in the yellow area.

Since the applied power for each damage caused to the paint is known, then it is possible to remove the corresponding additive phase from the calibration presented in the reference of Figure 29 simply subtracting the average value of the phase map (phase piston) from the power being worked with that of interest. The aforementioned is, if the additive phase map of the calibration is constant, it will be enough to also remove that constant value from the phase map of the measured three-dimensional form; in this case the damage caused by the optical trap. Once confirmed that the ratio is constant, it is possible to make a projection using the equation of straight line ($y = mx + C$) and the phase piston is given by $\Delta y = y_2 - y_1 = m(x_2 - x_1)$; being $C$ a constant that in this case is 0.204 and $m$ the slope that in this case is 0.0789. If the additive phase map were not constant, then a correction should be implemented by relating both phase maps, point to point. Figure 31 shows the Figure 30d phase map; from 0 to 4.78 μm corresponds to the uncorrected phase and the half from 4.78 to 10.27 μm is the

corrected measurement. It can be observed, in the corrected half, how the area of the paint that has not been damaged by the optical trap (areas colored in blue) remains with values close to those in Figure 30a. It is expected that the correction in each of the other phases will behave in the same way.

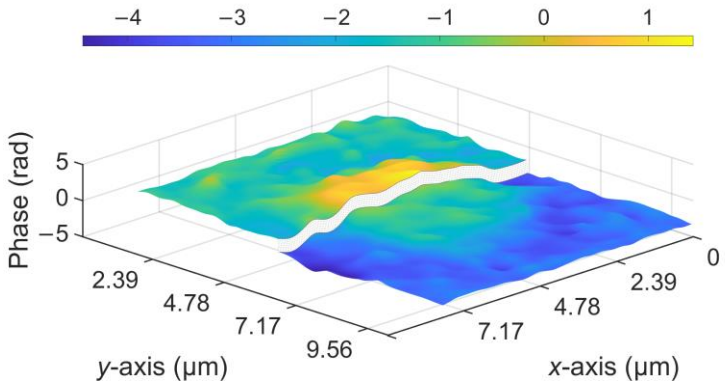


**Figure 31.** Measurement correction of the phase map at 205 mW of power. Left side (from 0 to 4.78 µm over the *y*-axis) corresponds to the uncorrected phase and the right side (from 4.78 to 10.27 µm) is the corrected measurement.

# *VI.*

# *Conclusions*

Starting from the observation of a phase shifting only by changing radiation power, the components of the experimental setup that could generate this optical contribution were studied. Taking advantage of the type of configuration, it was discarded that it were due to a mechanical effect. Then, it was determined that the media through which light travels in the setup should be analyzed. Chapter IV details how each media was evaluated and concludes the influence of the immersion oil on the phase measurements. These results were not found in the literature, which is a technical contribution to be considered in future works.

With the data presented here, it can be established that the additive phase piston detected in the optical trap is a consequence of changes in the immersion oil. Although in section IV.I.I (Figure 16d), the refractive index shows a Gaussian behavior, in Chapter V (Figure 27 and Figure 28), a quasi-constant phase shifting appears throughout the field of view, this due to the difference of orders of magnitude of the observed areas (mm and μm, respectively). This phase piston is attributed to a thermal effect caused by laser radiation when transmitted through immersion oil. Although the oil's morphological change (volume) does not usually affect the experiment directly, because it does not touch the sample under test, the change in temperature implies a variation in the refractive index and indicates an alteration in the beams focal point at the exit of the immersion objective used. In the experiments described in sections IV.I.I-III, the effect of a specific wavelength was analyzed, this was only to understand the oil behavior; if other wavelengths were used, it is suggested that there would be similar results, but with different ratios. Here, how immersion oil responds to different laser powers at wavelengths of 405, 532, and 976 nm is discussed. Also, the results could vary with a focused beam instead of the collimated beam used in those experiments. However, the calibration and phase correction were done with the trap's IR laser. Moreover, no phase shifting was identified with white LED light, suggesting that, as it is an extended source and is not coherent, it does not enough to heat the oil. In the case of a proper digital correction, the laser characteristics and the oil response to its exposure must to be known.

When an oil immersion objective is used in an interferometric measurement system that undergoes laser power changes, an additive phase term caused by the immersion oil reaction will be present. This effect occurs when coupling an interferometer and an optical trap, the latter is used to manipulate the object under test that the interferometer will measure. To obtain a correct measurement from the interferometer, that additive phase term must be removed from the measurement. In this study is demonstrated that the immersion oil, which is required by the microscope objective, is the component that reacts to the change in laser power, causing a phase shifting in the observed interferograms. Therefore, the immersion oil was analyzed optically, thermally and volumetrically, independent of the trap-interferometer setup. It was concluded that when there is a change in the laser source, it is necessary to calibrate the additive phase term in the trap-interferometer setup, to subsequently remove it from the measurements, as presented in Chapter V.

The direct applications of this study impact microscopes that use immersion oil and are used to measure a certain parameter (e.g. in the field of biology or micromanipulation). As well, since during the useful life of a laser, the power decreases, it would be necessary to implement the calibration described herein on a periodic basis. Another calibration would imply characterizing the ray convergence point of an oil immersion microscope objective, depending on the application and the equipment used. For example, for techniques such as microscopic interferometry, digital holographic microscopy or 3D flow cytometry, the phase term added by the change in the oil refractive index would have to be considered. In the same sense, for an optical trap or a confocal microscope, there

would be a change in the system's optical geometry. More robust work concerning the optical, thermal and morphological behavior of the material discussed here is left open.

It is reiterated that the time-dependent change in volume corresponds to the change in temperature and refractive index, since oil expands with heat. In addition, as the laser power increases, the WD decreases, the trap gradient force is higher, the oil is excited, and the oil's $n$ decreases; thus, there is a piston in the phase maps.

# *VII.*

# *Future Work*

Thin films are generally used to improve the surface properties of the substrates where they are deposited. To mention a few properties that can change are color, transmission, reflection, absorption, hardness, corrosion, permeability, electrical behavior and coefficient of friction, while the substrate shape remains virtually unchanged [56,57].

Thin film technology is categorized according to its manufacturing process: PVD (physical vapor deposition) and CVD (chemical vapor deposition). In turn, micro-, nano- and optoelectronics are derived from this technology, as well as nanotechnology [56].

Specifically, no thickness range has been determined for a film to be considered "thin". In practice, thin film technology and physics work with films from one layer of atoms (tenths of a nanometer) to a few micrometers thick. [57,58].

It is commonly understood that the properties of a three-dimensional material are not related to its volume. However, when the thickness of a thin film approaches just a few atomic layers, the proximity of two surfaces significantly influences the internal physical properties and processes of the material [58]; now adopting the term "two-dimensional material". Two-dimensional materials form an intermediate system between macrosystems and molecular systems, which opens up lines of research on the microphysical nature [58,59]. The most representative of these materials is graphene. It is considered graphene when there are less than ten atomic layers of graphite [4,5,60,61]. In this case, each layer has a crystalline structure of carbon atoms covalently bonded together in the form of a honeycomb [4,5,60,61]. In each honeycomb, a carbon-carbon bond length of ~0.142 nm is defined [5,61–63]. A graphene monolayer has been reported to have and a thickness of ~0.335 nm [64–66]. Graphene is also considered to be the basis for describing other carbonaceous materials such as fullerenes, nanotubes, graphite, etc [4,59]. Multiple techniques have been used to characterize the properties of the two-dimensional materials, such as the atomic force microscope (AFM) [59,63,67], X-Ray diffraction (XRD) [59,63,67,68], X-Ray photoelectron spectroscopy (XPS) [69], transmission electron microscopy (TEM) [63,67,68], scanning tunneling microscopy (STM) [70], Raman spectroscopy [59,60,63,67–69], UV-Visible spectroscopy [67,68], laser-induced breakdown spectroscopy (LIBS) [71], polarization indirect microscopic imaging (PIMI) [72], second harmonic generation (SHG) [73], third harmonic generation (THG) [73] and diamond anvil cell (DAC) [74], among many others. Some of the most relevant properties of graphene are the electronic [5,70], magnetic [60], thermal [70], optical [70] and mechanical [61,70]. Several models have been used to describe the mechanical behavior of graphene [5,66]; this is not trivial due to the difficulty of handling the material, as it has no stiffness in orders of micrometers and is considered practically invisible (it has a transmittance of 97.7%) [5,75,76] independent of wavelength [76,77].

Previous work has analyzed the mechanical behavior of graphene using specialized software, e.g., it have been done using linear finite element simulations of an atomistic model to analyze in-plane stresses of a graphene monolayer and a graphene bilayer [62]. But, in the case of the VMD (Visual Molecular Dynamics) software [78], in spite of being free, it is necessary to have the three-dimensional coordinates of each atom in a .pdb (protein data bank) file and some user experience in the handling of these type of computational packages for an adequate simulation. Due to the above, and for simplicity, it was decided to use JSME Molecular Editor [79] to model a monolayer of graphene (Figure 32).

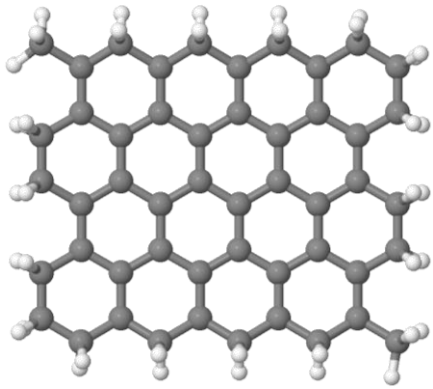

**Figure 32.** Graphene monolayer model with JSME Molecular Editor software.

For a more adequate characterization, it is important to know the material under study (the number of layers, purity, structure, etc.) [70]. Among the graphene production methods reported in the literature are mechanical exfoliation on an adhesive substrate [4], the metal-assisted exfoliation transfer onto PET substrates [80], the liquid-phase exfoliation [81], the CVD graphene film transferred onto glass substrates [82], the electrochemical delamination and transfer onto poly(methyl methacrylate) (PMMA) substrates [83,84] and the multiple bubbling techniques [85].

In this thesis, it is proposed to use the optical trap system to adapt the laser fragmentation in liquids technique [86] to fragment exfoliated graphene (EG) flakes suspended in water. This sample is also called solution-processed graphene suspended in water (SPGSW) by Guerra-Him [87].

Taking advantage of the optical trap configuration, suspended graphene flakes were used as a sample. According to Li's review [86], where it is mentioned that when there is laser ablation in liquids, a plasma phase is observed in a fraction of a second and then the material nanoparticles (NPs) are dispersed in the liquid medium. As a contribution of this work, the plasma phase in a powder suspension (in this case EG flakes) was observed. In contrast to what has been reported in the literature, our experimental setup has a large numerical aperture objective and a variable power laser. It is proposed as a method of mass production of graphenic materials, with the advantages of controlling the laser power and its focal point. On the other hand, it has the disadvantages that this method would be very slow since the ablation target would be one particle at a time and the evaporation time of the liquid medium is only a few minutes. In Figure 33 it is shown the described process of nanoparticles generation with this technique.

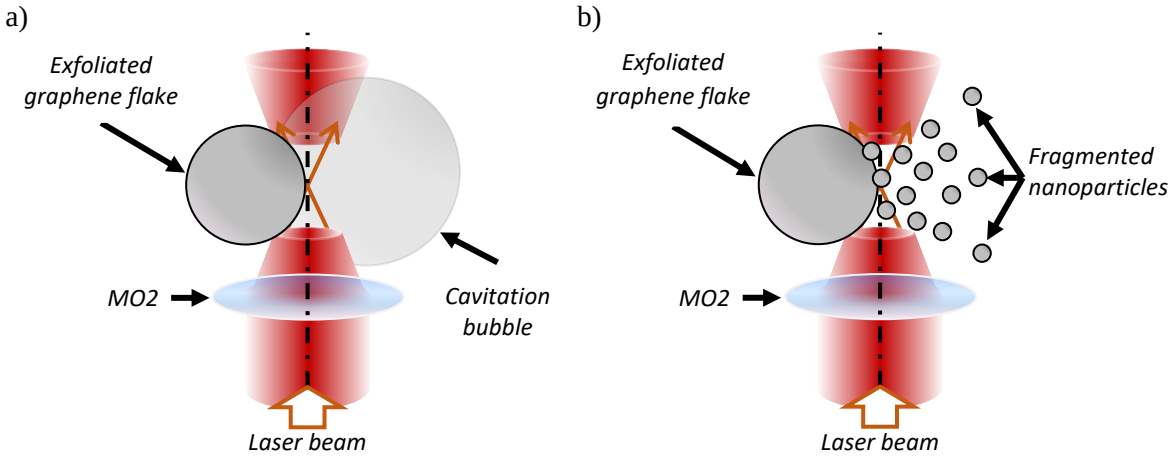


**Figure 33.** Phases of laser fragmentation of exfoliated graphene flakes suspended in water. a) Cavitation bubble generation, b) Fragmented nanoparticles generation.

EG melting is discarded, since it has been calculated to have a melting point above 4,000 K [88]. Figure 34 shows the fragmentation process of a particle when it is exposed at different laser powers. It was noticed that, when focusing the beam on a flake, a bubble of this material was generated. If the beam power is increased, this bubble bursts, thus fragmenting the material and producing the graphene nanoparticles that would later be characterized. This bubbling effect is of interest to us, as it was not observed in other samples in this and other works, such as the paint film and red blood cells, respectively. Of course, if the sample is not immersed in a liquid, only the plasma phase and fragmentation will be observed. A possible application of the generated particles could be as a dopant for other materials, but their properties would need to be analyzed. A more in-depth analysis of this method will be left for future work.

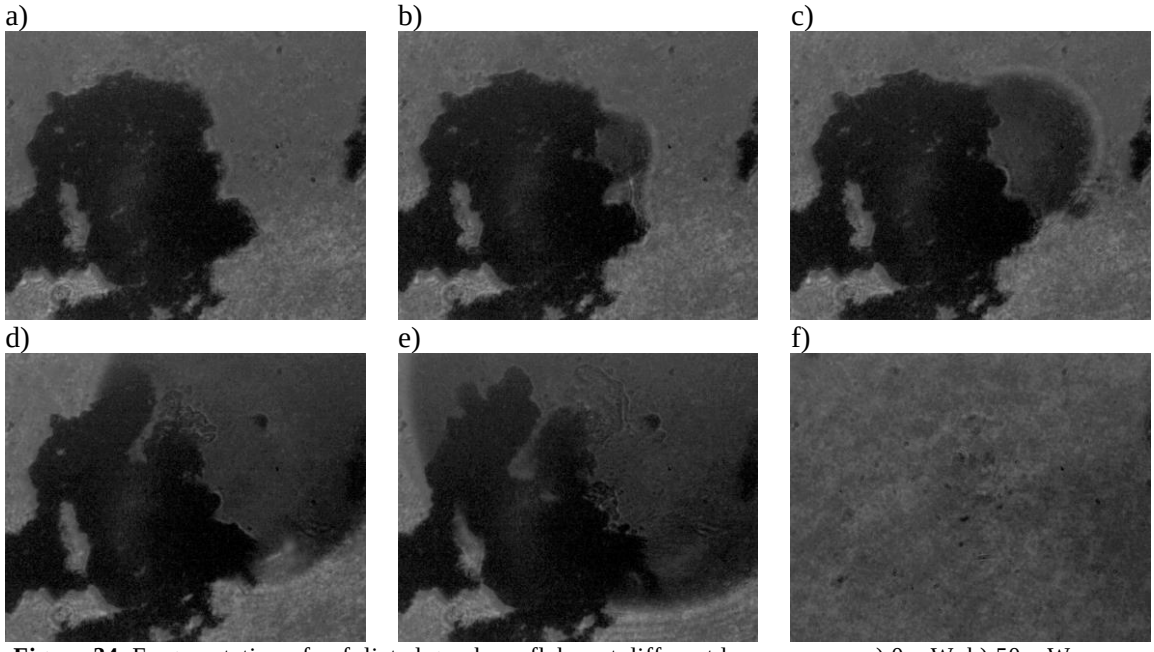


**Figure 34.** Fragmentation of exfoliated graphene flakes at different laser powers. a) 0 mW, b) 50 mW, c) 60 mW, d) 90 mW, e) 150 mW, f) 300 mW.

# References


[1] Ashkin, A. (1970) Acceleration and Trapping of Particles by Radiation Pressure. *Physical Review Letters*, **24**, 156–9. https://doi.org/10.1103/PhysRevLett.24.156

[2] Padgett, M.J., Molloy, J.E. and McGloin, D. (2010) Optical Tweezers: Methods and Applications. CRC Press.

[3] Tassieri, M. (2016) Microrheology with optical tweezers: Principles and applications. Microrheology with Opt. Tweezers Princ. Appl. Pan Stanford Publishing Pte. Ltd. https://doi.org/10.4032/9789814669191

[4] K. S. Novoselov et al. (2004) Electric Field Effect in Atomically Thin Carbon Films. **306**, 666–9. https://doi.org/10.1126/science.1102896

[5] Wolf, E.L. (2014) Applications of Graphene: An Overview. SpringerBriefs Mater. Springer. https://doi.org/10.1007/978-3-319-03946-6

[6] Fernández Arteaga, Y. (2017) Derivados grafénicos para el ensamblado de celdas OPVs a base de PTB7:PC71BM, Tesis de Maestría. Disponible en línea [https://cio.repositorioinstitucional.mx/jspui/bitstream/1002/356/1/17273.pdf]. Centro de Investigaciones en Óptica, A.C.

[7] Peña, R.A.Z. (2017) Novel Optical Eects in Functionalized Graphene: Formalism and Simulations. Centro de Investigaciones en Óptica.

[8] Morales-Narváez, E., Hassan, A. and Merkoçi, A. (2013) Graphene Oxide as a Pathogen-Revealing Agent: Sensing with a Digital-Like Response. *Angewandte Chemie*, **125**, 14024–8. https://doi.org/10.1002/ange.201307740

[9] Morales-Narváez, E. and Merkoçi, A. (2012) Graphene oxide as an optical biosensing platform. *Advanced Materials*, **24**, 3298–308. https://doi.org/10.1002/adma.201200373

[10] Dominguez Flores, A.D. (2019) Caracterizacion Mecanica de Materiales Compuestos Mediante Interferometria de Moteado de Desplazamiento Lateral, Tesis de Maestría. Disponible en línea [https://cio.repositorioinstitucional.mx/jspui/bitstream/1002/1086/1/17624.pdf]. Centro de Investigaciones en Óptica, A.C.

[11] Fujimura, T., Haketa, K., Hotta, M. and Kitahara, T. (2007) Global and systematic demonstration for the practical usage of a direct in vivo measurement system to evaluate wrinkles. *International Journal of Cosmetic Science*, **29**, 423–36. https://doi.org/10.1111/j.1468-2494.2007.00399.x

[12] Martínez, A., Rayas, J.A., Cordero, R.R., Balieiro, D. and Labbe, F. (2012) Leaf cuticle topography retrieved by using fringe projection. *Optics and Lasers in Engineering*, **50**, 231–5. https://doi.org/10.1016/j.optlaseng.2011.08.011

[13] Rayas, J.A. (2017) Desarrollo e implementación de un microscopio interferencial dual con trampa óptica para análisis morfológicos tridimensionales, Tesis de Doctorado. Disponible en línea [https://usach.primo.exlibrisgroup.com/permalink/56USACH_INST/172ual0/alma991885718606116]. Universidad de Santiago de Chile.

[14] Reyes, A.K. (2022) Sistema de pinzas ópticas mediante interferometría, Tesis de Doctorado. Disponible en línea [https://cio.repositorioinstitucional.mx/jspui/bitstream/1002/1261/1/18250.pdf]. Centro de Investigaciones en Óptica, A.C.

[15] Malacara, D. (1989) Óptica básica. México, D.F.

[16] Hecht, E. (2002) Optics. Addison-Wesley.

[17] Pedrotti, F.L., Pedrotti, L.S. and Pedrotti, L.M. (2007) Introduction to Optics.

[18] Sirohi, R.S. (2009) Optical methods of measurement: Wholefield techniques. CRC Press.

[19] Sharma, K. (2006) Optics: principles and applications. American Press.

[20] Hariharan, P. (2003) Optical interferometry. Academic Press.

[21] Servín, M., Quiroga, J.A. and Padilla, M. (2014) Fringe Pattern Analysis for Optical Metrology: Theory, Algorithms, and Applications. Wiley-VCH.

[22] Flores, V.H., Reyes-Figueroa, A., Carrillo-Delgado, C. and Rivera, M. (2020) Two-step phase

shifting algorithms: Where are we? *Optics and Laser Technology*, **126**. https://doi.org/10.1016/j.optlastec.2020.106105
[23] Kreis, T. (2004) Handbook of Holographic Interferometry. Wiley.
[24] Servin, M., Malacara, D., Marroquin, J.L. and Cuevas, F.J. (1997) Complex linear filters for phase shifting with very low detuning sensitivity. *Journal of Modern Optics*, **44**, 1269–78. https://doi.org/10.1080/09500349708230736
[25] Malacara, D., Servín, M. and Malacara, Z. (2005) Interferogram Analysis for Optical Testing. Second Edi. CRC Press.
[26] Montalvo Arenas, C.E. (2010) Microscopía [http://bct.facmed.unam.mx/wp-content/uploads/2018/08/2_microscopia.pdf].
[27] Bradshaw, D.S. and Andrews, D.L. (2017) Manipulating particles with light: Radiation and gradient forces. *European Journal of Physics*, IOP Publishing. **38**, 34008. https://doi.org/10.1088/1361-6404/aa6050
[28] Maragò, O.M., Jones, P.H., Gucciardi, P.G., Volpe, G. and Ferrari, A.C. (2013) Optical trapping and manipulation of nanostructures. *Nature Nanotechnology*, Nature Publishing Group. **8**, 807–19. https://doi.org/10.1038/nnano.2013.208
[29] Zhang, H. and Liu, K.K. (2008) Optical tweezers for single cells. *Journal of the Royal Society Interface*, **5**, 671–90. https://doi.org/10.1098/rsif.2008.0052
[30] Ashkin, A. (1992) Forces of a single-beam gradient laser trap on a dielectric sphere in the ray optics regime. *Biophysical Journal*, Elsevier. **61**, 569–82. https://doi.org/10.1016/S0006-3495(92)81860-X
[31] Ren, Y.-X., Wu, J.-G. and Li, Y.-M. (2011) Application of Monte Carlo Simulation in Optical Tweezers. *Applications of Monte Carlo Method in Science and Engineering*, InTech. p. 950. https://doi.org/10.5772/14542
[32] Kress, H., Stelzer, E.H.K., Griffiths, G. and Rohrbach, A. (2005) Control of relative radiation pressure in optical traps: Application to phagocytic membrane binding studies. *Physical Review E - Statistical, Nonlinear, and Soft Matter Physics*, **71**, 1–10. https://doi.org/10.1103/PhysRevE.71.061927
[33] Reihani, S.N.S. and Oddershede, L.B. (2007) Improving optical trapping in the axial direction and a continuous change of the optimal trapping depth. *Optical Trapping and Optical Micromanipulation IV*, **6644**, 664421. https://doi.org/10.1117/12.733622
[34] Kaňok, R., Ciprian, D. and Hlubina, P. (2018) Sensing of liquid analytes via the phase shift induced by surface plasmon resonance. *Optical Sensing and Detection V*, **10680**. https://doi.org/10.1117/12.2305718
[35] Mahmoudi, A. and Reihani, S.N.S. (2011) The effect of immersion oil in optical tweezers. *Optics Express*, **19**, 14794. https://doi.org/10.1364/oe.19.014794
[36] Gieseler, J., Gomez-Slano, J.R., Magazzù, A., Pérez Castillo, I., Pérez García, L., Gironella-Torrent, M. et al. (2021) Optical Tweezers: A Comprehensive Tutorial from Calibration to Applications. *Advances in Optics and Photonics*, **13**, 74–241. https://doi.org/10.1364/AOP.394888
[37] Celliers, P.M. and Conia, J. (2000) Measurement of localized heating in the focus of an optical trap. *Applied Optics*, **39**, 3396–407. https://doi.org/10.1364/ao.39.003396
[38] Butola, A., Popova, D., Prasad, D.K., Ahmad, A., Habib, A., Tinguely, J.C. et al. (2020) High spatially sensitive quantitative phase imaging assisted with deep neural network for classification of human spermatozoa under stressed condition. *Scientific Reports*, Nature Publishing Group UK. **10**, 1–12. https://doi.org/10.1038/s41598-020-69857-4
[39] Liu, Z., Wu, J., Zhang, Y., Zhang, Y., Tang, X., Yang, X. et al. (2018) Optical trapping and axial shifting for strongly absorbing particle with single focused TEM00 Gaussian beam. *Applied Physics Letters*, **113**, 0–5. https://doi.org/10.1063/1.5044463
[40] Reihani, S.N.S. and Oddershede, L.B. (2007) Optimizing immersion media refractive index improves optical trapping by compensating spherical aberrations. *Optics Letters*, **32**, 1998. https://doi.org/10.1364/ol.32.001998
[41] Richardson, A.C., Reihani, N. and Oddershede, L.B. (2006) Combining confocal microscopy with precise force-scope optical tweezers. *Optical Trapping and Optical Micromanipulation*

*III*, **6326**, 632628-1 632628-10. https://doi.org/10.1117/12.680347
[42] Matrecitos-Avila, M., Avila, R., Pimentel-Domínguez, R., Cuevas, S., Tamariz, E. and Loza-Alvarez, P. (2022) Focus variation due to near infrared laser in a confocal microscope. *Microscopy Research and Technique*, **85**, 3431–8. https://doi.org/10.1002/jemt.24198
[43] Baxter, C. and Loudon, R. (2010) Radiation pressure and the photon momentum in dielectrics. *Journal of Modern Optics*, **57**, 830–42. https://doi.org/10.1080/09500340.2010.487948
[44] Bradshaw, D.S. and Andrews, D.L. (2017) Manipulating particles with light: Radiation and gradient forces. *European Journal of Physics*, IOP Publishing. **38**, 17. https://doi.org/10.1088/1361-6404/aa6050
[45] Burns, T.M., Preece, D., Niemenen, T.A. and Rubinsztein-Dunlop, H. (2013) Optical tweezers for precise control of micro-bubble arrays: in situ temperature measurement. *Optical Trapping and Optical Micromanipulation X*, **8810**, 1–11. https://doi.org/10.1117/12.2024254
[46] Chow, K.W., Preece, D. and Berns, M.W. (2017) Effect of red light on optically trapped spermatozoa. *Biomedical Optics Express*, **8**, 6. https://doi.org/10.1364/boe.8.004200
[47] Gao, D., Ding, W., Nieto-Vesperinas, M., Ding, X., Rahman, M., Zhang, T. et al. (2017) Optical manipulation from the microscale to the nanoscale: Fundamentals, advances and prospects. *Light: Science and Applications*, Nature Publishing Group. **6**. https://doi.org/10.1038/lsa.2017.39
[48] Dawood, F., Qin, S., Li, L., Lin, E.Y. and Fourkas, J.T. (2012) Simultaneous microscale optical manipulation, fabrication and immobilisation in aqueous media. *Chemical Science*, **3**, 2449–56. https://doi.org/10.1039/c2sc20351k
[49] Grier, D.G. (2003) A revolution in optical manipulation. *Nature*, **424**, 810–6. https://doi.org/10.1038/nature01935
[50] Pollari, R. and Milstein, J.N. (2015) Improved axial trapping with holographic optical tweezers. *Optics Express*, **23**, 28857. https://doi.org/10.1364/oe.23.028857
[51] Nedev, S., Urban, A.S., Lutich, A.A. and Feldmann, J. (2011) Optical force stamping lithography. *Nano Letters*, **11**, 5066–70. https://doi.org/10.1021/nl203214n
[52] Ombinda-Lemboumba, S., Malabi, R., Lugongolo, M.Y., Thobakgale, S.L., Manoto, S. and Mthunzi-Kufa, P. (2017) Investigation of HIV-1 infected and uninfected cells using the optical trapping technique. *Biophysics, Biology and Biophotonics II: The Crossroads*, **10075**, 100750M. https://doi.org/10.1117/12.2252294
[53] Habaza, M., Gilboa, B., Roichman, Y. and Shaked, N.T. (2015) Tomographic phase microscopy with 180° rotation of live cells in suspension by holographic optical tweezers. *Optics Letters*, **40**, 1881–4. https://doi.org/10.1364/ol.40.001881
[54] Cargille-Laboratories. (2018) Immersion Oil Type LDF [https://cargille.com/wp-content/uploads/2018/11/Immersion-Oil-Type-LDF.pdf].
[55] Ibidi. (2020) Ibidi µ-Slide I Luer [https://ibidi.com/channel-slides/50--slide-i-luer.html#product-details].
[56] Frey, H. and Khan, H.R. (2015) Handbook of Thin-Film Technology. Springer.
[57] IEC. (2016) Thin Film Technology. Int. Electrotech. Vocab.
[58] Eckerttová, L. (1977) Physics of Thin Films. https://doi.org/10.1007/978-1-4615-7589-4
[59] Gupta, A., Sakthivel, T. and Seal, S. (2015) Recent development in 2D materials beyond graphene. *Progress in Materials Science*, Elsevier Ltd. **73**, 44–126. https://doi.org/10.1016/j.pmatsci.2015.02.002
[60] Pati, S.K., Enoki, T. and Rao, C.N.R. (2011) Graphene and Its Fascinating Attributes. WORLD SCIENTIFIC.
[61] Wolf, E.L. (2014) Graphene: A New Paradigm in Condensed Matter and Device Physics. Informa UK Limited.
[62] Khandoker, N., Islam, S. and Hiung, Y.S. (2017) Finite element simulation of mechanical properties of graphene sheets. *IOP Conference Series: Materials Science and Engineering*, **206**. https://doi.org/10.1088/1757-899X/206/1/012057
[63] Cao, C., Wu, X., Xi, X., Filleter, T. and Sun, Y. (2014) Handbook of Nanomaterials Properties. *Handbook of Nanomaterials Properties*, 121–35. https://doi.org/10.1007/978-3-642-31107-9_35

[64] Blakslee, O.L., Proctor, D.G., Seldin, E.J., Spence, G.B. and Weng, T. (1970) Elastic constants of compression-annealed pyrolytic graphite. *Journal of Applied Physics*, **41**, 3373–82. https://doi.org/10.1063/1.1659428
[65] Lee, C., Wei, X., Kysar, J.W. and Hone, J. (2008) Measurement of the elastic properties and intrinsic strength of monolayer graphene. *Science*, **321**, 385–8. https://doi.org/10.1126/science.1157996
[66] Berinskii, I.E. and Borodich, F.M. (2013) Elastic in-plane properties of 2D linearized models of graphene. *Mechanics of Materials*, Elsevier Ltd. **62**, 60–8. https://doi.org/10.1016/j.mechmat.2013.03.004
[67] Liu, W.-W., Chai, S.P., Mohamed, A.R. and Hashim, U. (2014) Synthesis and characterization of graphene and carbon nanotubes: A review on the past and recent developments. *Journal of Industrial and Engineering Chemistry*, Elsevier B.V. **20**, 1171–85. https://doi.org/10.1016/j.jiec.2013.08.028
[68] Sahu, S.R., Devi, M.M., Mukherjee, P., Sen, P. and Biswas, K. (2013) Optical property characterization of novel graphene-X (X=Ag, Au and Cu) nanoparticle hybrids. *Journal of Nanomaterials*, **2013**. https://doi.org/10.1155/2013/232409
[69] Jia, C., Jiang, J., Gan, L. and Guo, X. (2012) Direct optical characterization of graphene growth and domains on growth substrates. *Scientific Reports*, **2**, 1–6. https://doi.org/10.1038/srep00707
[70] Madhuri, S. and Maheshwar, S. (2015) Graphene: An introduction to the fundamentals and industrial applications. Wiley.
[71] Serrano, J., Cabalín, L.M., Moros, J. and Laserna, J.J. (2014) Potential of laser-induced breakdown spectroscopy for discrimination of nano-sized carbon materials. Insights on the optical characterization of graphene. *Spectrochimica Acta - Part B*, Elsevier B.V. **97**, 105–12. https://doi.org/10.1016/j.sab.2014.05.003
[72] Liu, X., Qiu, B., Chen, Q., Ni, Z., Jiang, Y., Long, M. et al. (2014) Characterization of graphene layers using super resolution polarization parameter indirect microscopic imaging. *Optics Express*, **22**, 20446–56. https://doi.org/10.1364/oe.22.020446
[73] Kaplas, T., Karvonen, L., Ahmadi, S., Amirsolaimani, B., Mehravar, S., Peyghambarian, N. et al. (2016) Optical characterization of directly deposited graphene on a dielectric substrate. *Optics Express*, **24**, 2965–70. https://doi.org/10.1364/oe.24.002965
[74] Akinwande, D., Brennan, C.J., Bunch, J.S., Egberts, P., Felts, J.R., Gao, H. et al. (2017) A review on mechanics and mechanical properties of 2D materials—Graphene and beyond. *Extreme Mechanics Letters*, Elsevier Ltd. **13**, 42–77. https://doi.org/10.1016/j.eml.2017.01.008
[75] Huang, H. and Huang, J. (2014) Organic and Hybrid Solar Cells. Huang H, and Huang J, editors. J. Chem. Inf. Model. Springer.
[76] Weber, J.W., Calado, V.E. and Van De Sanden, M.C.M. (2010) Optical constants of graphene measured by spectroscopic ellipsometry. *Applied Physics Letters*, **97**, 1–3. https://doi.org/10.1063/1.3475393
[77] Nair, R.R., Blake, P., Grigorenko, A.N., Novoselov, K.S., Booth, T.J., Stauber, T. et al. (2008) Fine structure constant defines visual transparency of graphene. *Science*, **320**, 1308. https://doi.org/10.1126/science.1156965
[78] Schulten, K. (1995) Visual Molecular Dynamics (VMD) [https://www.ks.uiuc.edu/Research/vmd/].
[79] Bienfait, B. and Ertl, P. JSME Molecular Editor [https://biomodel.uah.es/en/DIY/JSME/draw.es.htm].
[80] Zaretski, A. V., Moetazedi, H., Kong, C., Sawyer, E.J., Savagatrup, S., Valle, E. et al. (2015) Metal-assisted exfoliation (MAE): Green, roll-to-roll compatible method for transferring graphene to flexible substrates. *Nanotechnology*, IOP Publishing. **26**, 45301. https://doi.org/10.1088/0957-4484/26/4/045301
[81] Mohd Yusoff, A.R. (2014) Graphene Optoelectronics: Synthesis, Characterization, Properties, and Applications. Wiley-VCH.
[82] Gong, J.R. (2011) Graphene – Synthesis, Characterization, Properties and Applications.

Graphene - Synth. Charact. Prop. Appl. InTech. https://doi.org/10.5772/22530
[83] Krajewska, A., Pasternak, I., Sobon, G., Sotor, J., Przewloka, A., Ciuk, T. et al. (2017) Fabrication and applications of multi-layer graphene stack on transparent polymer. *Applied Physics Letters*, **110**, 5. https://doi.org/10.1063/1.4974457
[84] Tang, Z., Neumann, C., Winter, A. and Turchanin, A. (2020) Electrochemical delamination assisted transfer of molecular nanosheets. *Nanoscale*, Royal Society of Chemistry. **12**, 8656–63. https://doi.org/10.1039/d0nr01084g
[85] Shi, Z., He, P., Wang, N., Liu, Y., Chen, X., Li, Y. et al. (2022) Bubble-Mediated Mass Production of Graphene: A Review. *Advanced Functional Materials*, **32**, 1–23. https://doi.org/10.1002/adfm.202203124
[86] Li, L., Zhang, J., Wang, Y., Uz Zaman, F., Zhang, Y., Hou, L. et al. (2021) Laser irradiation construction of nanomaterials toward electrochemical energy storage and conversion: Ongoing progresses and challenges. *InfoMat*, **3**, 1–29. https://doi.org/10.1002/inf2.12218
[87] Guerra-Him, A., Fernández-Arteaga, Y., Maldonado, J.L., Valle-Orta, M., Sierra, U., Fernández, S. et al. (2023) Implementation of an alternative graphene-based electrode. *Journal of Materials Science: Materials in Electronics*, **34**. https://doi.org/10.1007/s10854-023-09901-x
[88] Ganz, E., Ganz, A.B., Yang, L.M. and Dornfeld, M. (2017) The initial stages of melting of graphene between 4000 K and 6000 K. *Physical Chemistry Chemical Physics*, **19**, 3756–62. https://doi.org/10.1039/c6cp06940a

# Appendix A: Achievements

## PEER-REVIEWED PUBLISHED PAPERS

Domínguez-Flores, A.D.; Rayas, J.A.; Martínez-García, A.; Cordero, R.R.; "Analysis and Correction of the Additive Phase Effect Generated by Power Change in a Mach–Zehnder Interferometer Integrated to an Optical Trap" ***Appl. Sci.*** 2024, 14, 2404.

## EDITORIAL ACTIVITY (JOURNAL REVIEWER)

OPTICA Publishing Group

IEEE Transactions on Instrumentation & Measurement

IOP Publishing Group

## NATIONAL AND INTERNATIONAL CONFERENCES

**11/2023** Juan A. Rayas, Azael D. Domínguez-Flores and Amalia Martínez García. *Calibration of the phase contribution generated by the optical excitation of the immersion oil in an interferometer and optical trap system*. MOPM (Mexican Optics and Photonics Meeting) (México).

**06/2023** Azael David Domínguez Flores, Juan Antonio Rayas Alvarez and Amalia Martínez García. *Effect of laser radiation on the refractive index of an oil immersion objective*. Siegman International School on Lasers (Ireland).

**07/2022** Azael David Domínguez Flores and Juan Antonio Rayas Alvarez. *Mechanical characterization of two-dimensional materials using optical tweezers: Additive phase effect interferometric study generated by the change of luminous intensity in an optical trap*. CIO's Graduate Student Poster Session. Guanajuato (México).

**08/2021** Azael David Domínguez Flores and Juan Antonio Rayas Alvarez. *Mechanical characterization of two-dimensional materials using optical tweezers*. CIO's Graduate Student Poster Session. Guanajuato (México).

## ATTENDED MEETINGS

**10/2023** FiO LS Conference

**10/2023** Student Leadership

**06/2023** Siegman International School on Lasers

**05/2023** Women in science meeting

**09/2022** Women in science meeting

**10/2020** OSA Laser Congress meeting ONLINE (COVID situation)

**09/2020** FiO + LS Conference meeting ONLINE (COVID situation)

**08/2020** "Luz estructurada y visión computacional 3D" meeting ONLINE (COVID situation)

**08/2020** Express Conference on the Physics of Materials and its application in Energy and Environment meeting ONLINE (COVID situation)

**07/2020** Advanced Photonics meeting ONLINE (COVID situation)

**06/2020** Imaging and Applied Optics / Optical Sensors and Sensing meeting ONLINE (COVID situation)

## GUEST TALKS & SEMINARS:

**12/05/2023** Guest talk "Midiendo con luz" (Measuring with light). Congreso "Fotónica: La Tecnología de la Luz". Jalisco (México).

**08/06/2021** Guest talk "El uso de la luz para medir la altura de objetos" (Use of light to measure the height of objects) El Instituto Politécnico Nacional a través del Centro de Estudios Científicos y Tecnológicos 17. Guanajuato (México).

**28/04/2021** Guest talk "El uso de la luz para medir la altura de objetos" (Use of light to measure the height of objects) El Tecnológico Nacional de México a través del Instituto Tecnológico Superior de Irapuato. Guanajuato (México).

## OUTREACH EXPERIENCE

**08/09/2023** "La ciencia también es cosa de mujeres: Encuentro entre chicas y científicas" (Sience is also a women's thing: A meeting between girls and female scientists).

Organizer in the 6$^{th}$ edition of this event, which have the purpose of motivate high-school woman students to study a science career.

**08/07/2023** Guest guide for visits to the "Ana María Cetto" museum and the "Manuel Peimbert Sierra" planetarium.

**12/05/2023** Photography (scientific and artistic category) & short-story contest.

Organizer in the contest titled "A look into the invisible".

**17/03/2023** Visit of Dr. Alessandra Carmichael-Martins (2022 Optica Ambassador) and Dr. Francisco Javier Gantes (Traveling Lecturer) to the Centro de Investigaciones en Óptica, A.C.

General Chair of this event, where both guests participated in a lecture for CIO students and researchers on their current work and in a talk exclusively for student chapter members focused on professional development and mental health awareness.

**03/03/2023** Workshop Facilitator in the social appropriation of science workshop "InspecCIOnando al micromundo" (Inspecting the microworld) of the "Connecting the Mexican Bioimaging Community" program in the Mexican Bioimaging Workshops 4 meeting.

**25/11/2022** Speaker in the Science Fair of the Escuela de Nivel Medio Superior Centro Histórico León (ENMSCHL-UG).

**25/03/2022 & 11/11/2022** "La ciencia también es cosa de mujeres: Encuentro entre chicas y científicas" (Sience is also a women's thing: A meeting between girls and female scientists).

| | |
|---|---|
| | Organizer in the 4th and 5th edition of this event, which have the purpose of motivate high-school woman students to study a science career. |
| **12/09/2022-05/10/2022** | Staff in the 1st Braille Basic Workshop as a part of The Meeting for the Education in Science for the Inclusion (ENECI, for its acronym in Spanish). |
| **30/06/2022** | Participating in the UNITEC's (Universidad Tecnológica de México) cultural week with an astronomical observation and science/engineering workshops for highschool and undergraduate students. |
| **23/05/2022** | Photography (scientific and artistic category) & short-story contest. |
| | Organizer in the contest titled “Beyond the visible”. |
| **28/04/2022** | Representing the CIO with the workshop "Nada es lo que parece; Ilusiones ópticas" (Nothing is what it seems; Optical Illusions) in the VII Festival of Arts, Sciences and Humanities which was organized by the UNAM (National Autonomous University of Mexico), León Unit. |
| **26/03/2022** | Leader of the workshop "Máquinas de Agua" (Water Machines) as a part of the "Iluminando el Futuro" initiative. |
| **16/11/2021** | Anthology “International day of LGBTQIA people in STEM” |
| | Working on promotion of this anthology. We share some illustrated biographies of scientists who have contributed to the creation of spaces for the LGBTQIA+ community in STEM. |
| | https://issuu.com/ciochapter/docs/english_lgbtqistem_ilustbio?fbclid=IwAR0gyefaA2b_VfdmkaylTpEvXgDvVbCkGGU8kdRdiqYoqDM5u9LVdgISFbA |
| **26/02/2021** | “La ciencia también es cosa de mujeres: Encuentro entre chicas y científicas” (Sience is also a women’s thing: A meeting between girls and female scientists). |
| | Organizer in the 3rd edition of this event, which have the purpose of motivate high-school woman students to study a science career. |
| **28/02/2020 &** | “La ciencia también es cosa de mujeres: Encuentro entre chicas y científicas” (Sience is also a women’s thing: A meeting between girls and female scientists). |
| **06/03/2020** | Organizer of this event (1st & 2nd edition), which had the purpose of motivating high-school woman students to pursue a career in science. 100 participants had the opportunity to participate in talks and workshops, and to visit laboratories at CIO. The event was organized by CIO-OPTICA-SPIE Student Chapter and CIO. |
| **01/2019-to date** | Coffee W/Science, |
| | Promoter & organizer in this monthly meeting, which is one of the most innovative activities that we have implemented with CIO-OPTICA-SPIE Student Chapter. We invite a researcher (local or foreign) to talk about his/her experience in a field of science/research, and to give advice to students who pursue a career in optics and photonics, all of it while sharing a cup of coffee. |
| **2018-to date** | Officer in the CIO Student Chapter of OPTICA (formerly OSA). |

Treasurer (2023)

President (2022)

We organize activities to promote scientific knowledge among our local community. We organize series of seminars, talks and contests, as well as outreach and professional development events.

**2018-2023** Officer in the CIO Student Chapter of SPIE.

We organize activities to promote scientific knowledge among our local community. We organize series of seminars, talks and contests, as well as outreach and professional development events.

## SCHOLARSHIPS

| | |
|---|---|
| Zuegel Family Scholarship to attend the *Siegman International School on Lasers*, 2023. | OPTICA (formerly OSA) |